Energy & Buildings 361 (2026) 117500

Contents lists available at ScienceDirect

Energy & Buildings

journal homepage: www.elsevier.com/locate/enb

Explainable machine-learning surrogates for sun-patch-driven indoor thermal comfort

Reda Snaiki [a], Abdelatif Merabtine [a,*], Shengqiang Shi [b], Ines Grabaa [a]

[a] *Department of Construction Engineering, École de Technologie Supérieure, Université du Québec, Montréal, Québec, Canada*
[b] *Laboratory of Mechanical & Material Engineering, Université de Technologie de Troyes, Troyes, France*

ARTICLE INFO

Keywords:
Thermal comfort
Sun patch
Machine learning
Hydronic radiant floor
Local discomfort
Explainable AI (SHAP)

ABSTRACT

Localized solar patches generate transient indoor thermal asymmetries that conventional steady-state models cannot adequately capture, particularly in environments conditioned by radiant floor systems. Under these circumstances, the heated slab is subjected to additional radiative loading, which can exacerbate thermal comfort risks by inducing localized overheating. This study develops interpretable data-driven surrogate models to predict the short-term evolution of global and local thermal comfort in an experimental 1:1 test chamber equipped with a hydronic floor system. Using a 'delta-prediction' strategy to capture system dynamics, seven machine learning algorithms are trained to predict Body Average Comfort (BAC), Body Average Sensation (BAS), and local temperatures near the head and ankle over a 10-minute horizon. Ensemble tree-based and kernel-based models regression generally outperformed linear baselines, achieving high generalization on an independent test period: R^2 reached 0.97 for ankle temperature ($RMSE \approx 0.32$℃), 0.93 for BAS, and 0.85 for BAC. Head temperature proved the most challenging target ($R^2 \approx 0.81$, $RMSE \approx 1.36$℃) due to complex radiative interactions. Grouped SHAP analysis reveals distinct physical drivers: while global comfort is dominated by operative temperature and humidity, direct solar radiation is the overwhelming driver of local temperatures and a significant contributor to thermal sensation. A counterfactual Sun Patch Impact (SPI) analysis quantifies this effect, showing that solar exposure systematically elevates predicted sensation by up to 0.05 scale units at peak irradiance (800 W/m^2). Finally, a principal component analysis identifies a 'local–global mismatch' phenomenon, where 18–20% of globally neutral states conceal local overheating risks at the ankle level, highlighting the necessity of multi-objective monitoring for effective sun-patch management.

1. Introduction

Radiant heating and cooling (RHC) systems are increasingly deployed in high-performance buildings to enhance thermal comfort while reducing energy consumption and exergy destruction [1–3]. Unlike conventional air-based systems, RHC systems condition large-area surfaces via mainly hydronic circuits, fundamentally reshaping the indoor radiant surfaces and creating spatially non-uniform thermal environments [4,5]. This approach offers advantages in highly glazed perimeter zones where solar gains are prominent, yet simultaneously introduces complex thermal dynamics that challenge traditional comfort assessment frameworks [6].

The widely adopted PMV/PPD framework recommended in ISO 7730 [7] and ASHRAE 55 [8] relies on steady-state heat balance assumptions and group-average thermal sensation under spatially uniform conditions. However, multiple field studies and systematic reviews have documented limited predictive accuracy for PMV in non-uniform, stratified, or transient environments [9,10]. These limitations arise because the steady-state formulation cannot adequately capture the physiological and psychological responses to local radiation variations, vertical air temperature stratification, temporal fluctuations in thermal boundary conditions, individual thermal history and adaptation, and occupant control affordances. The predictive gap is particularly pronounced in radiant and displacement ventilation systems where mean radiant temperature (MRT) becomes a primary determinant of occupant comfort.

When RHC systems are deployed in highly glazed facades, moving sun patches introduce a dominant exogenous disturbance that challenges both comfort maintenance and control strategies [1,4,5,11–14]. Solar radiation creates localized radiative loading on conditioned slabs,

---

* Corresponding author at: Department of Construction Engineering, École de Technologie Supérieure, Université du Québec, Montréal, Québec, Canada.
E-mail address: abdelatif.merabtine@etsmtl.ca (A. Merabtine).

https://doi.org/10.1016/j.enbuild.2026.117500
Received 16 December 2025; Received in revised form 16 March 2026; Accepted 16 April 2026

producing elevated floor surface temperatures, enhanced vertical stratification, and thermal persistence effects. Controlled experiments report floor surfaces reaching 32–34 °C during extended sun-patch exposure (6 h, approximately 718 W/m^2), exceeding the ISO 7730 comfort limit of 29 °C [15]. Sun patches elevate upper-body temperatures relative to ankle height, potentially shifting environments from ISO Category A to Category B for vertical temperature difference [15]. Due to slab thermal inertia, local overheating and stratification can persist well beyond direct solar exposure, complicating reactive control strategies. Field measurements and bi-climatic chamber studies document indoor air temperatures exceeding 26 °C in winter during sun-patch events, with documented correlations among sun-patch area, radiant system outlet temperature, and occupant-reported thermal sensation [12,13,15]. Thermal manikin studies reveal that prolonged solar exposure creates combined vertical and lateral asymmetries that affect body-segment temperatures differentially, with ankle and head temperatures serving as critical indicators of local discomfort.

The literature converges on four critical findings. First, steady-state global comfort indices inadequately represent transient, non-uniform thermal conditions of radiant systems in stratified or sun-exposed environments. Second, moving sun patches constitute a dominant disturbance driving local overheating, vertical stratification, and thermal discomfort that persists due to thermal inertia. Third, while standards provide essential local discomfort criteria, emerging experimental evidence suggests these limits exhibit context-dependent flexibility, particularly for vertical gradients under whole-body neutral conditions. Fourth, dynamic, interpretable models coupled with solar- and occupancy-aware control logic are necessary to operationalize comfort maintenance under realistic operating conditions.

A parallel body of literature has examined thermal discomfort caused by direct solar radiation, radiant asymmetry, and sun-patch effects in highly glazed spaces and in buildings equipped with radiant systems. Marino et al. [11] showed that solar radiation can substantially affect local indoor thermal comfort through its impact on radiant temperature asymmetry. Benzaama et al. [16] investigated the transient effect of sun patches on heated floors and highlighted the importance of accounting for sun-patch evolution in thermal analyses. Dong et al. [17] combined numerical and experimental approaches to assess the effect of solar radiation on indoor thermal comfort in radiant-heating conditions. More recently, Shi et al. [12]experimentally evaluated the impact of a real moving sun patch on radiant floor heating and thermal comfort, while Shi et al. [4] reviewed solar-driven overheating in buildings with radiant systems and emphasized the need for more rigorous assessment of comfort degradation under highly glazed conditions. Field evidence reported by Hwang et al. [18] also showed that indoor thermal comfort near façades is strongly affected by solar irradiation and spatial position. Collectively, these studies establish the physical importance of direct solar exposure, localized discomfort, and transient floor- and near-window effects.

Recognizing the inadequacy of steady-state models for transient, non-uniform conditions, researchers have increasingly adopted machine learning (ML) and hybrid physics-ML approaches. A systematic review by Qavidel et al. [19] demonstrates that ML comfort models outperform PMV by up to 35% for group predictions and 74% for personalized models when properly feature-engineered and validated against subjective thermal sensation data. Moreover, ML-based control strategies have achieved comfort-related energy reductions of 20–58% compared to conventional setpoint-based approaches. In the literature, a range of ML algorithms have been applied to predict thermal comfort and local discomfort, with ensemble models consistently outperforming traditional approaches. Among them, Artificial Neural Networks (ANNs) has shown a strong effectiveness for predicting mean radiant temperature and comfort indices (e.g., PMV, SET), with high accuracy ($R^2 > 0.9$) [20–22]. Random Forest (RF) & Support Vector Machines (SVM) improve accuracy by 38.6% and SVM by 50% when spatial parameters are included; both outperform traditional PMV models [23,24]. Ensemble Models (XGBoost, LightGBM, CatBoost) achieve superior accuracy in predicting comfort votes, with mean radiant temperature and air temperature as key features [25,26]. Rahmanparast et al. [27] have shown that Ensemble ML models predict comfort indices with up to 96% accuracy using fewer input parameters, outperforming PMV models. In addition, many authors have performed comparative performance studies in which it has been shown that RF and stacking models improve accuracy by 9.5–49.4% over other methods; ML-based MPC achieves up to 39.1% energy savings while maintaining comfort [28–31]. According to [28,32] ML-based MPC and ensemble models offer better generalization and robustness, especially in environments with radiant floors and dynamic solar gains.

The integration of spatial–temporal data and building morphology is critical for accurate, dynamic prediction and control. ML models, particularly ensemble approaches, have demonstrated the ability to substantially improve the prediction of thermal comfort and local discomfort in complex, sun patch-affected environments [21,23,25,27,28,33–35]. However, practical implementation faces several challenges, including representative data collection across diverse occupants and conditions, appropriate temporal resolution and prediction horizons, feature selection encoding relevant physics (radiation, stratification, thermal history), model generalization across buildings and seasons, and post-occupancy validation. However, the main challenge with these ML models is the lack of “interpretability”. The “black box” nature of many ML algorithms complicates the design-decision process for radiant systems in sun-exposed spaces, particularly when models must account for short-term solar radiation forecasts, vertical temperature profiles, directional radiation metrics, and asymmetry effects. To bridge this gap, successful ML approaches should be transparent to designers and researchers. Deploying “Explainable” ML techniques, such as SHAP (SHapley Additive exPlanations), offers a robust solution. Explainable AI (XAI) has emerged as an important complement to predictive modeling, because comfort-related building decisions require not only accurate predictions but also physically interpretable reasoning. SHAP enables the quantification of the contribution of each input feature to model predictions, offering both global and local interpretability [36–39]. By visualizing domain knowledge, these techniques enhance transparency and trust [37,40], revealing how ML models capture complex spatial effects and non-linear interactions that traditional statistical approaches often miss [38].

SHAP has been used to assess thermal sensation by interpreting hybrid XGBoost and Bayesian optimization models, identifying key factors and interactions affecting individual comfort [41,42]; and to reveal the influence of solar radiation and environmental factors on comfort and air quality models [43]. Integrating SHAP with tree-based ensemble models and rule-based controllers enhances interpretation of nonlinear effects between solar radiation, floor temperature, and occupant sensation according to [44,45]. Combining SHAP with multi-objective optimization and ensemble learning clarifies nonlinear and interaction effects among variables (e.g., shading, solar radiation, environmental conditions) according to [46–49]. Integrating occupant feedback, physiological data, and environmental sensing with SHAP enhances transparency and supports adaptive HVAC control as stated by Gugliermetti et al. [50]. Liu and Ma [51] developed an explainable thermal comfort evaluation model using Bayesian-optimized LightGBM and SHAP, showing how SHAP can be used to interpret feature effects in building thermal-comfort evaluation. Zhang et al. [52] used infrared thermography together with explainable AI to analyze occupant thermal state prediction, while Kim et al. [53] proposed an interpretable general thermal comfort model based on physiological data from wearable biosensors and SHAP analysis. More recently, Li et al. [54] extended SHAP-based analysis to dynamic thermal comfort estimation under temperature-ramp conditions using infrared-camera-derived features. These studies demonstrate clear progress in interpretable comfort modeling; however, they mainly address overall thermal evaluation, physiological sensing, or relatively general indoor conditions, rather than solar-driven spatial non-uniformity and localized body-level responses.

Despite their potential for enhancing trust and customization, SHAP and similar explainable methods remain underutilized for comfort assessment in sun patch/radiant floor settings [41,52,55]. Validated, interpretable predictive models that explicitly forecast both global and local comfort metrics (including near-body-segment temperatures) over short horizons under sun-patch transients in radiant systems are lacking. The intersection of sun patch effects, hydronic radiant floor systems, and explainable ML models represents a frontier in occupant-centric building design and operation. While ensemble ML models and SHAP-based interpretations have advanced the field, significant opportunities remain for integrating thermal comfort data, high-resolution sensing, and hybrid explainability frameworks to achieve truly adaptive, personalized, and energy-efficient thermal comfort management.

Despite these advances, the intersection between these two streams of research remains limited. On the one hand, XAI-based thermal comfort studies have improved transparency in machine-learning prediction, but they have generally focused on overall comfort states, physiological sensing, or global feature ranking [51,53,54]. On the other hand, sun-patch and radiant-asymmetry studies have established the physical importance of direct solar exposure and localized discomfort, but they have rarely been framed through explainable machine-learning surrogates that explicitly distinguish among localized outputs and changing solar regimes [12,16,56]. This leaves a clear gap for a framework that is not only predictive, but also able to reveal how the dominant drivers of comfort evolve between no-sun and sun-patch conditions, and how these changes differ between localized responses and integrated whole-body indices.

The present work addresses this gap by developing and validating interpretable ML surrogates for the short-term prediction of global thermal comfort and sensation indices, local comfort metrics (head and ankle temperatures), and vertical temperature gradients under sun-patch transients. Developed models are trained on experimental data from a 1:1 experimental test room equipped with a hydronic radiant floor heating system exposed to real sun patches to explicitly capture the coupled effects of solar forcing, thermal stratification, and system thermal inertia. First, it benchmarks various ML algorithms using a ‘delta-prediction’ strategy to capture the coupled dynamics of solar forcing and system inertia. Second, it deploys SHAP to decompose the black-box predictions into physically interpretable drivers, ranking the influence of radiant asymmetry versus background conditions. Finally, it introduces a model-based counterfactual metric, the Sun Patch Impact (SPI) index, and a ‘local–global mismatch’ diagnostic to quantify how often neutral global sensation masks potential local overheating. These tools collectively provide a framework for proactive, comfort-centric control in highly glazed, radiant-conditioned spaces.

2. Experimental procedure

Several experiments were conducted in a 1:1 experimental test cell facility to characterize the impact of transient sun patches on indoor thermal conditions and human thermal perception in radiant-heated spaces. The experimental dataset captures the dynamic interactions between direct solar exposure and the indoor environment under realistic operating conditions, providing a detailed representation of sun-patch-driven thermal non-uniformities. Measurements include boundary conditions, solar gains, hydronic floor operation, local air temperatures, and thermal responses. The following sections describe the experimental setup, instrumentation, and data acquisition procedures.

2.1. Description of the experimental test facility

All measurements were performed in a full-scale modular test cell located in an open outdoor environment, as shown in Fig. 1. The test cell is a compact, rectangular, highly insulated structure designed for controlled thermal experiments. Its south-facing facade incorporates two large and double-glazed windows that allow direct solar radiation to enter the space during the sunny days, enabling the formation of a well-defined sun patch on the interior floor. Its window-to-floor ratio (WFR) is 22.78%, which meets the current requirement recommending the WFR of new residential buildings to be higher than 16% [57]. The envelope is constructed with sandwich-panel walls to minimize unwanted heat transfer and to ensure a clear thermal response to solar gains.

The indoor environment is intentionally kept minimally furnished so that radiant exchange and the spatial evolution of the sun patch can be observed without interference from additional objects. A small mechanical ventilation unit is installed externally to provide controlled air exchange without imposing significant thermal loads. Hydronic pipes embedded within the floor slab supply radiant conditioning during the experiments, while the surrounding open field ensures unobstructed solar exposure and reduces external shading effects. The facade experiences strong incident solar radiation during clear-sky days, which creates a well-defined sun patch on the floor. The progression of this patch across the room during the day, both in intensity and in surface location, forms a key source of spatially non-uniform thermal loads, and serves as the physical driver underlying the machine-learning analysis.

From Fig. 2a, it can be observed that hydronic system adopts a circuit layout pattern of counter flow. All tubes are placed in the bottom of 6 cm thick slab. The system consists of two hydronic circuits: Circuit 1, located on the window-facing side of the room, and Circuit 2, positioned on the opposite side farther from the window. Circuit 1 and Circuit 2 are 69 m and 62 m long of crosslinked polyethylene tubes, respectively. The distance between pipes is approximately 15 cm. Water circulation in each loop is driven by a dedicated pump, and the two circuits operate in parallel to ensure uniform surface temperature distribution across the floor [58,59].

Heated water is supplied from a heat-pump-based hydronic loop (Fig. 2b). The heat pump is connected to a buffer tank that stabilizes temperature fluctuations and ensures continuous operation under varying loads. A three-way valve regulates whether the buffer tank water is directed toward the floor circuits or bypassed, enabling precise control of the inlet water temperature delivered to the test room. A flowmeter installed upstream of the floor slab monitors the total supply

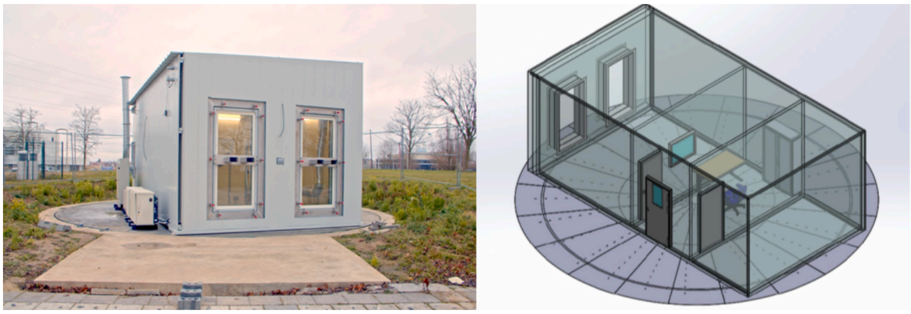

Fig. 1. Full scale experimental test cell exposed to real climatic conditions.

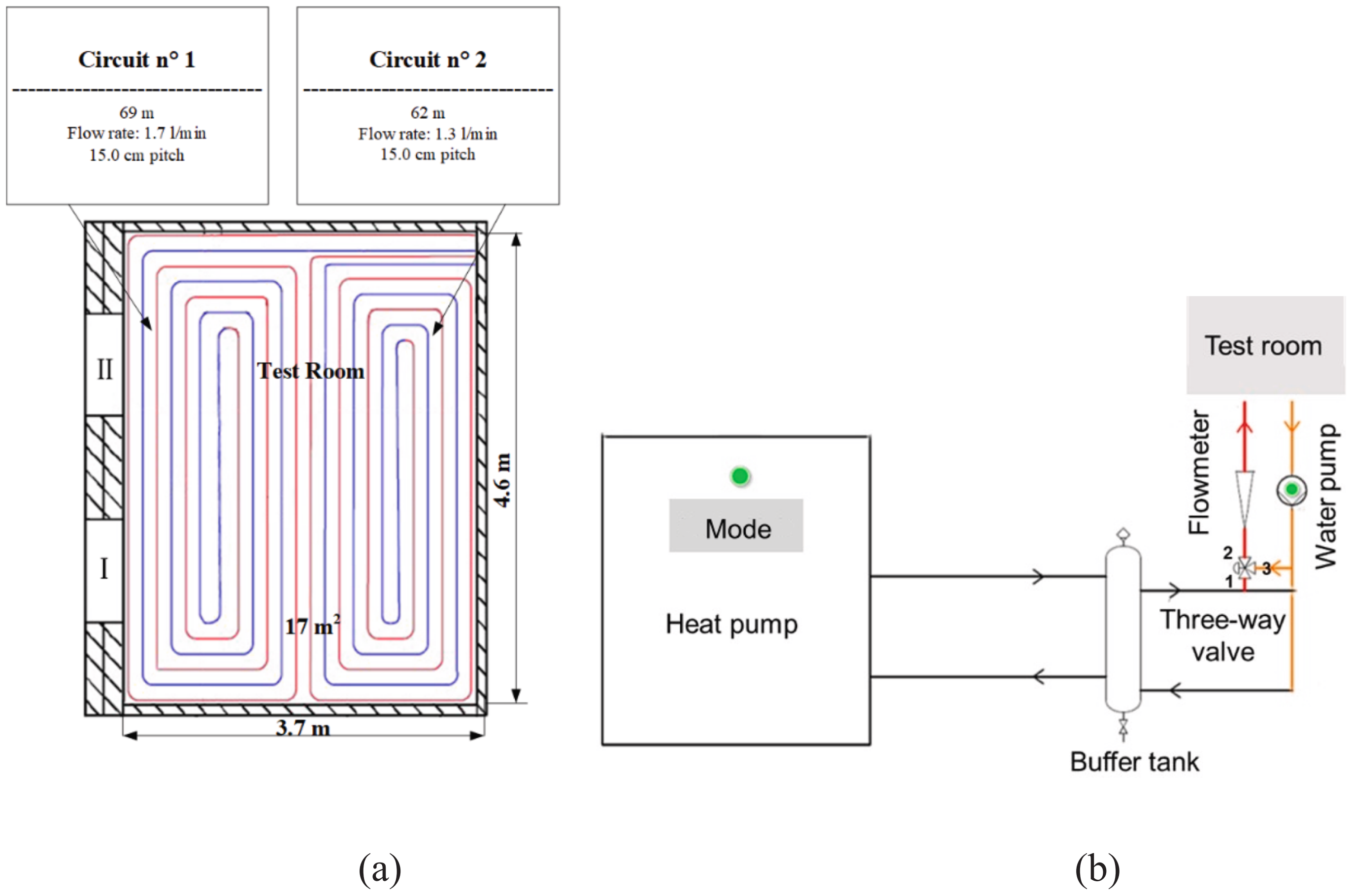

Fig. 2. HVAC systems. (a) floor heating system; (b) hydraulic circuit supplied by the heat pump.

flow. By adjusting the operating mode of the heat pump, the system can operate in either cooling or heating mode, although only heating operation was used in the present study to investigate sun-patch-driven overheating. A small mechanical ventilation unit provides a constant fresh-air flow for air renewal only, without introducing any thermal conditioning. This ensures that no air-side heat input affects the experiment, so that the observed indoor temperature and thermal comfort variations can be attributed mainly to the hydronic radiant floor and to the solar gains.

2.2. Monitoring

A detailed sensor network was deployed inside and around the test room to capture the thermal and environmental conditions governing sun-patch-driven comfort dynamics (Fig. 3). The monitoring includes surface temperature probes, air temperature and humidity sensors, water temperature sensors for both hydronic circuits, and outdoor boundary-condition sensors. All signals were recorded at fixed 10-minute intervals during the experimental campaign. The same 10-minute time step was later adopted in the surrogate modelling, so that the machine-learning models operate directly on the experimental sampling grid without additional temporal resampling.

Previous studies on radiant systems and sunlit spaces have shown that surface temperatures provide a sensitive indicator of both hydronic floor operation and localized solar loading. Other studies have shown that no significant thermal gradients occur when the system operates without solar influence [59]. Therefore, based on these observations, five surface temperature sensors were strategically distributed across the floor to capture the onset and propagation of thermal non-uniformities induced by sun-patch exposure. Sensors 1, 2, and 5 were aligned with the two window zones, where direct beam radiation enters, and the local surface temperature is expected to vary most strongly. Sensors 3 and 4 were positioned between the window-facing regions to monitor the transition from sunlit to shaded zones. This configuration ensures that both high-gradient areas and background regions are adequately represented. All sensors are surface-mounted thermocouples with fast response time, enabling detailed tracking of local temperature gradients associated with the hydronic circuit layout and the advancing sun patch.

Five sensor trees equipped with air temperature and relative humidity sensors were installed inside the test room. Each sensor tree was positioned 15 cm away from the corresponding surface measurement point, with all sensors mounted at a height of 1.68 m. This height represents the head level of a standing person and is used as a reference for the indoor air-state conditions. For subsequent analysis, indoor relative humidity was defined as the spatially averaged value across the sensor trees, providing a representative room-scale moisture state.

A combined PT100 air temperature probe and capacitive humidity sensor was mounted on the east wall at 1.12 m height, corresponding to the standard reference level for thermal comfort studies. This sensor provides the indoor air temperature used as the feedback variable in the PID controller regulating the inlet-water temperature of the hydronic floor system. Its location was selected to be representative of the room air conditions while remaining outside the direct solar beam, so that the control signal is not biased by local sun-patch heating.

The radiant floor consists of two independent circuits, each equipped with its own inlet and outlet temperature sensors: Inlet temperature sensor (7), Outlet temperature sensor (9) for Circuit 1 (window-side loop); Inlet temperature sensor (8), Outlet temperature sensor (10) for Circuit 2 (opposite-side loop).

These sensors measure the hydronic system's thermal input and

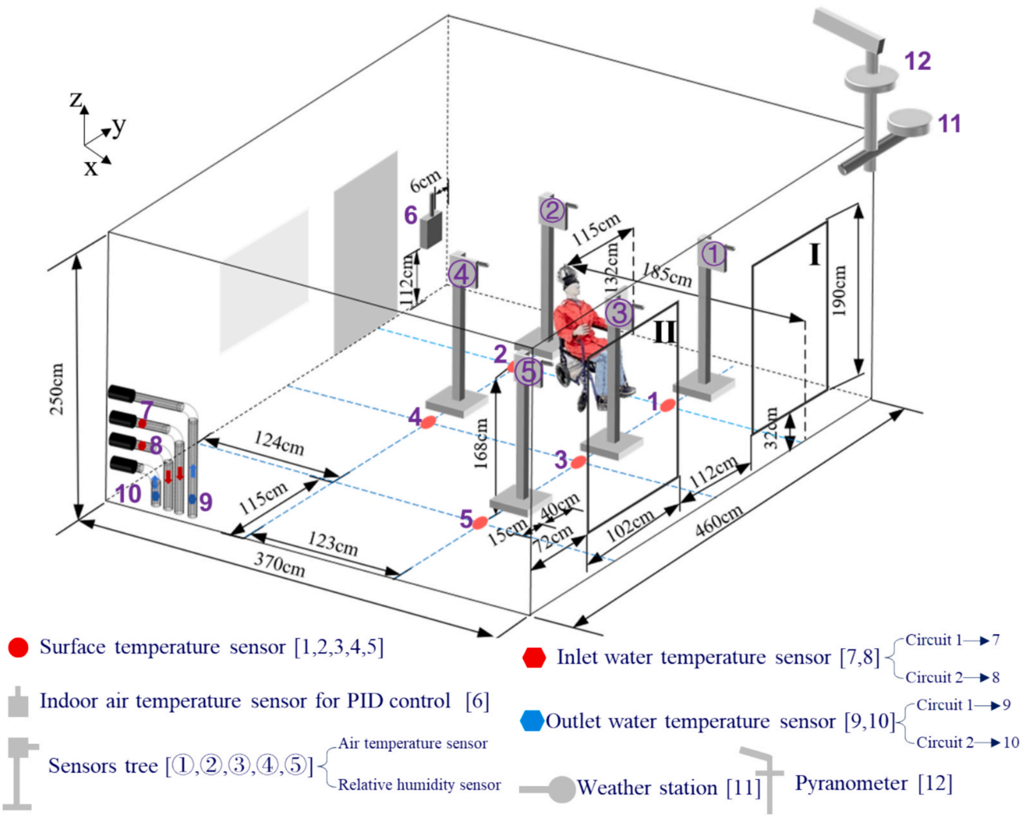

Fig. 3. Monitoring layout of the experimental test cell.

extraction rates. The inlet temperature acts as the primary control variable, while the outlet temperature reflects the heat exchange occurring within each circuit. Recording both circuits separately enables detailed interpretation of floor-surface temperature differences and reveals how solar loading interacts with the water loops.

A Weather station (11) was installed to measure outdoor air temperature, relative humidity, and wind speed, forming the boundary conditions for heat exchange through the envelope. Additionally, a pyranometer (12) mounted on a south-facing boom and aligned with the glazing plane records direct solar radiation, the key driver of sun-patch formation. Only the direct beam component was used in the analysis, as diffuse radiation does not produce a localized patch.

All sensors were connected to a centralized data-logging platform with synchronized timestamps using NTP correction at the beginning of each measurement day.

2.3. *Thermal manikin-based comfort assessment*

Thermal comfort responses were obtained using a full-scale thermal manikin (Newton, Thermetrics®), which provides controlled, repeatable, and ethically unconstrained measurements under transient and thermally non-uniform conditions. The manikin is seated inside the test room during all experimental periods as shown in Fig. 4.

The Thermal Manikin Newton consists of 34 independently controlled thermal zones, each equipped with embedded heating elements and high-precision skin temperature sensors. This configuration allows the manikin to reproduce human metabolic heat release and to respond to environmental transients in a physiologically meaningful manner. Local air temperatures at different heights were measured using thermistors mounted directly on the thermal manikin. According to ISO 7730 [7], temperature probes were positioned at the manikin's head (1.1 m) and ankle level (0.1 m) to capture the contrasting thermal environments produced by solar exposure and radiant heating. These two heights correspond to the primary local comfort targets used in Section 3, with the ankle-level temperature being particularly sensitive to the advancing sun patch and the head-level temperature reflecting vertical stratification and convective behavior. A relative humidity sensor and an air velocity sensor were placed on the shoulder to monitor the local micro-environment around the manikin. Together, these measurements

Fig. 4. Seated thermal Manikin Newton®.

provide the multi-level thermal environment required to interpret localized comfort responses under transient and non-uniform solar conditions.

A dedicated control and acquisition system, consisting of a J-Box interface, a power enclosure, and proprietary software, regulates the heat output of each zone and records all thermal variables at 10-minute intervals. This system allows the manikin to simulate the physiological responses of typical humans [60,61]. More details about the manikin are provided in Refs. [13,59,62,63].

The thermal manikin used in this study adopts the human thermal comfort model proposed by Zhang (2003), and the thermal comfort and sensation scales are shown in Table 1 (Zhang, 2003) [64].

Zhang's model predicts local and overall sensations, and then local and overall comfort in non-uniform thermal conditions. Local thermal sensation S_{local} is represented by a function of core temperature and local skin temperature and their changes (see equation (1)). The skin and core temperatures represent the response to the stable condition, and the derivatives account for the transient feature. The overall thermal sensation $S_{overall}$ is a weighted average of all the local sensations (see equation (2)). The overall sensation and thermal comfort are calculated by means of the core temperature and the local skin temperatures, and their variation over time.

$$S_{local} = 4\left(\frac{2}{1+e^{-C_1\left(T_{skin,local}-T_{skin,local,set}\right)-K_1\left[\left(T_{skin,local}-T_{\overset{\cdots}{skin}}\right)-\left(T_{skin,local,set}-T_{\overset{\cdots}{skin}}\right)\right]}}-1\right)+C_{2i}\frac{dT_{skin,local}}{dt}+C_{3i}\frac{dT_{core}}{dt} \tag{1}$$

$$S_{overall} = \frac{\sum\left(w_i S_{local,i}\right)}{w_i} \tag{2}$$

where S_{local} is Local sensation; C_1 is Body-part specific regression coefficients; $T_{skin,local}$ is Local skin temperature, ℃; $T_{skin,local,set}$ is Local skin set-point temperature, ℃; K_1 is Body-part specific regression coefficients; $T_{\overset{\cdots}{skin}}$ is Mean body skin set point temperature, ℃; C_2 is Body-part specific regression coefficients; C_3 is Body-part specific regression coefficients; i is segment; T_{core} is Core temperature; $S_{overall}$ is Overall sensation; w_i is Weighting factor.

Local thermal comfort is predicted using a logistic (sigmoid) function of local sensation and overall sensation as follows:

$$C_i = -\frac{1}{1+exp(\alpha_i S_i + \beta_i S_{overall})} \tag{3}$$

where C_i is local thermal comfort (-4 very uncomfortable to $+4$ very comfortable) and α_i and β_i are empirically fitted coefficients.

Table 1
Thermal comfort and sensation scales.

Thermal comfort	Scale	Thermal sensation	Scale
Very Uncomfortable	−4	Very Cold	−4
Uncomfortable	−2	Cold	−3
Just Uncomfortable	0-	Cool	−2
Just Comfortable	0+	Slightly Cool	−1
Comfortable	+2	Neutral	0
Very Comfortable	+4	Slightly Warm	+1
		Warm	+2
		Hot	+3
		Very Hot	+4

Overall thermal comfort is expressed as:

$$C_{overall} = \frac{C_{min1}+C_{min2}}{2} \tag{4}$$

C_{min1} and C_{min2} are the two most uncomfortable local comfort votes.

And for transient or controlled environments:

$$C_{overall} = \frac{C_{min1}+C_{min2}+C_{max}}{2} \tag{5}$$

C_{max} is the most comfortable local vote.

For each time step, the model evaluates the real-time skin temperature distribution, metabolic heat release, and predicted thermoregulatory signals across the manikin's 34 independently controlled thermal zones. The whole-body indices are computed by aggregating the local responses from all zones, yielding body-average quantities that reflect the combined thermal state of the full-body system. The model outputs two indices: (i) Body Average Sensation (BAS) representing whole-body thermal sensation on a − 4 to + 4 scale (Very Cold to Very Hot); and (ii) Body Average Comfort (BAC) representing the hedonic comfort evaluation on a continuous bipolar scale from "very uncomfortable" to "very comfortable".

Both indices evolve with the dynamic environment created by radiant heating, solar gains, and sun-patch movement. BAS reacts rapidly to environmental forcing, while BAC incorporates slower, perceptual-level modulation. These two indices constitute the subjective comfort targets of the surrogate models developed in Section 3. Since the models predict changes ΔBAS(t) and ΔBAC(t), the manikin outputs were recorded at a 10-minute resolution to capture transient effects during sun-patch exposure.

2.4. *Sun-patch characterization*

Direct solar radiation entering through the facade produces a spatially localized sun patch whose intensity and movement depend on solar angle and sky conditions. Although no direct imaging system was used, the sun patch was characterized implicitly through the direct beam radiation signal, the known window geometry and orientation, and the observed time periods of localized temperature rise at ankle/head levels.

During clear-sky periods, the sun patch appeared on the floor shortly after local noon and progressed gradually across the occupied zone over a 3- to 5-hour period. Its geometric progression leads to clear temporal hysteresis between solar input and resulting local temperatures, a pattern later captured by the time-lagged ML features in Section 3 and manifested in the SPI hysteresis scatters.

2.5. *Experimental protocol*

The experiments were meticulously designed to generate a high-resolution, time-series dataset capturing the transient thermal responses and comfort dynamics driven by localized solar patches within a radiant-conditioned test cell. This protocol ensures the data fidelity required for training and evaluating the short-horizon machine-learning surrogate models.

The test room was maintained under controlled operating conditions: the indoor air temperature set point was fixed at 20℃; the hydronic floor heating system was initially activated to heat the radiant slab until the indoor air temperature reached the set point and attained a thermal steady state; A PID controller regulated the floor inlet water temperature, using the indoor air temperature measured by Sensor 6 as the feedback variable.

At the beginning of each scenario, the system was activated to warm the slab until the room reached 20 °C and steady conditions were established. After this initial phase, the radiant floor did not operate continuously. Instead, the PID controller adjusted the water pump and the three-way mixing valve according to the deviation from the setpoint: when indoor air temperature fell below 20 °C, warm water was circulated through the slab; when indoor temperature exceeded the setpoint, typically due to solar gains, the controller reduced the flow rate or fully closed the valve. This feedback-driven, intermittent operation ensured that the day-to-day and intra-day thermal dynamics observed inside the test room were dominated by the intensity and duration of the sun patch rather than by variations in system input.

A small mechanical ventilation unit provided constant fresh-air flow solely for air renewal, ensuring no air-side heat input influenced the experiment. The test cell employed a half-shading setup for all scenarios, with Window I opened and Window II closed, facilitating the formation of a single, distinct sun patch on the floor. The manikin was seated and preheated, with its 34 independently controlled zones set to optimal temperatures corresponding to the 20 ℃ room temperature, allowing it to simulate human metabolic heat release and adapt to the dynamic environment. The manikin's proprietary data acquisition system recorded the following four comfort-related targets, which serve as the outputs (y_{t+1}) for the ML models: BAC, BAS, Temperature near the ankle (Local air temperature at 0.1 m height), Temperature near the head (Local air temperature at 1.1 m height). All sensors and the manikin's data acquisition system were synchronized, and raw data were resampled to a fixed 10-minute interval. This uniform sampling grid directly defines the short-horizon for the one-step-ahead Δ-prediction models ($\Delta y_t = y_{t+1}$-y_t). The experiments spanned seven days across three distinct scenarios, primarily focused on the West orientation to investigate sun-patch-induced overheating even in sub-optimal winter orientations. The complete dataset was partitioned into training and independent test periods to assess the ML model generalization in Table 2.

During the test days (Scenario 3), the independent nature of the data ensures that the reported predictive performance (R^2 and RMSE) is an accurate measure of the surrogate models' ability to generalize to unseen, real-world transient conditions.

3. Explainable machine learning surrogate model

3.1. Problem formulation

The primary objective of this study is to develop data-driven surrogate models capable of predicting the short-term evolution of thermal comfort within spaces exposed to dynamic solar loads. Dynamic solar patches introduce transient and spatially heterogeneous thermal conditions that conventional steady-state models, such as Fanger's PMV/PPD framework, are not designed to accurately assess the resulting discomfort risk. To address this limitation, the present study aims to predict both whole-body thermal comfort indices and localized temperature variations, with particular emphasis on vertical gradients, as well as the risk of thermal stress, recognized by international standards (ISO 7730, ASHRAE 55) as critical factors influencing occupant dissatisfaction. Importantly, the term 'global thermal comfort' in this context refers not to space- or time-averaged metrics, but to the integrated thermal sensation of the entire body. This was achieved using a 34-segment thermal manikin, enabling high-resolution assessment of local thermal conditions across body regions, which were subsequently aggregated to derive a comprehensive whole-body thermal comfort measure. To comprehensively assess these dynamics, four target variables (referred to hereafter as thermal comfort-related variables) are considered:

Table 2
Detailed information on three different experimental scenarios.

Scenario	Day	Orientation	Rotation Applied	Data Function
1	March 27–30	West 270°	No	Training Period
2	April 9	West 270° → Northwest 300°	Yes (18:00–19:00)	Training Period (Rotation used to extend sun patch duration)
3	April 7–8	West 270°	No	Independent Test Period (Used for performance evaluation in Section 3.3)

1. Body Average Comfort (BAC): An aggregated whole-body metric representing the thermal comfort index of all 34 body segments.
2. Body Average Sensation (BAS): An aggregated whole-body metric reflecting the thermal sensation of all 34 body segments.
3. Temperature near the ankle: Measured at approximately 0.1 m above the floor.
4. Temperature near the head: Measured at approximately 1.1 m above the floor, corresponding to the height of a seated person.

In the machine learning model, the modeling framework does not directly regress the absolute future value y_{t+1}, to improve the robustness of the forecasting. Instead, the models are trained to predict the temporal increment, defined as:

$$\Delta y_t = y_{t+1} - y_t \tag{6}$$

This 'delta-prediction' strategy is mathematically advantageous for thermal time-series data. It prevents the models from exploiting the strong persistence inherent in thermal variables (where $y_{t+1} \approx y_t$, yielding a trivial baseline) and instead forces the learning algorithms to capture the rate of change induced by fluctuating boundary conditions. This approach is particularly relevant for quantifying the rapid impact of sun patches and hydronic floor system thermal response.

The input feature vector at time t is constructed to capture the physical state of the environment subject to external driving parameters. It comprises the outdoor air temperature (T_{out}), indoor operative temperature (serving as a proxy for the room's thermal state) (T_{op}) including implicitly mean radiant temperature and indoor air temperature, the mean inlet water temperature of the floor system (T_w), the direct solar radiation incident on the façade (G), and the mean indoor relative humidity (RH). Furthermore, to account for the thermal inertia of the building components and the delayed physiological responses of the body to radiative heat, the input vector is augmented with a tailored set of lagged values for both the predictors and the target variable. These lag structures extend between 6- and 12-time steps, depending on the specific inertia associated with each target variable. The models are trained on a dataset spanning multiple days with diverse solar and control conditions, for the same heating period, while performance is evaluated on an independent two-day testing period to ensure generalization.

3.2. Model families and training strategy

To identify the most effective surrogate for each thermal-comfort related variable, this study compared a diverse set of regression models spanning linear, kernel-based, and ensemble methods. The set of candidate models included linear approaches, Ridge and Elastic Net (EN) regression, to establish baselines for potential linear dependencies, as well as Support Vector Regression (SVR) with a radial basis function (RBF) kernel to capture non-linear relationships in a high-dimensional feature space. Furthermore, four ensemble tree-based architectures were evaluated to handle complex interactions and discontinuities: the Random Forest (RF) Regressor, Extra-Trees (ET) Regressor, Gradient Boosting Regressor (GBRT) utilizing Huber loss for robustness against outliers, and the histogram-based Gradient Boosting Regressor (HGBR) for computational efficiency.

All models were trained on the same delta-prediction dataset and evaluated independently for each target variable. Hyperparameter tuning was performed using a randomized search strategy coupled with a time-series cross-validation scheme (4 folds). This approach strictly preserves the temporal order of the data, thereby preventing data leakage from future observations into past training sets. Preprocessing requirements were tailored to the specific model architectures; for distance-based algorithms (Ridge, EN, and SVR), input features were standardized using a standard scaler within a pipeline, whereas tree-based models (RF, ET, GBRT, and HGBR) were trained directly on the original feature scales. The optimization metric during cross-validation was the Root Mean Squared Error of the increment (Δy). Final model performance was reported on the independent test period using both the coefficient of determination (R^2) and the RMSE calculated on the reconstructed absolute future value (y_{t+1}).

3.3. Predictive performance

Table 3 summarizes the performance of all six model families across the four thermal-comfort related variables. The results demonstrate that the proposed surrogate modeling approach yields robust predictions with high generalization capability. For BAC, all non-linear models achieved comparable performance, with test R^2 values ranging between 0.84 and 0.85 and RMSE of approximately 0.21 units. The RF regressor yielded the best generalization ($R^2 = 0.846$, $RMSE = 0.208$), followed closely by GBRT and SVR. Notably, linear models (Ridge and EN) proved slightly less accurate in this context, suggesting that non-linear interactions between solar radiation, inlet water temperature, and the indoor state play a non-negligible role in determining perceived comfort.

Table 3
Comparison of machine learning models for predicting comfort indices and local temperatures.

Target	Model	R^2 (Train)	RMSE (Train)	R^2 (Test)	RMSE (Test)
BAC	RF	0.914	0.256	0.846	0.208
	GBRT	0.900	0.276	0.843	0.210
	SVR	0.961	0.172	0.842	0.211
	EN	0.883	0.299	0.841	0.211
	ET	0.911	0.261	0.841	0.212
	HGBR	0.900	0.276	0.826	0.221
	Ridge	0.914	0.256	0.734	0.274
BAS	RF	0.983	0.078	0.924	0.087
	GBRT	0.982	0.080	0.927	0.085
	SVR	0.979	0.087	0.927	0.085
	EN	0.977	0.091	0.925	0.086
	ET	0.993	0.050	0.927	0.085
	HGBR	0.980	0.085	0.920	0.089
	Ridge	0.980	0.085	0.928	0.084
T_{ankle}	RF	0.987	0.303	0.965	0.336
	GBRT	0.988	0.286	0.967	0.328
	SVR	0.978	0.393	0.969	0.318
	EN	0.978	0.389	0.967	0.326
	ET	0.990	0.267	0.964	0.344
	HGBR	0.984	0.331	0.964	0.342
	Ridge	0.979	0.384	0.967	0.329
T_{head}	RF	0.984	0.559	0.800	1.403
	GBRT	0.984	0.567	0.796	1.418
	SVR	0.977	0.668	0.796	1.419
	EN	0.980	0.623	0.796	1.419
	ET	0.983	0.575	0.784	1.459
	HGBR	0.983	0.580	0.812	1.360
	Ridge	0.989	0.467	0.800	1.406

In contrast, BAS proved to be highly predictable across all model families, with test R^2 values consistently falling within the narrow range of 0.92–0.93 and RMSE values around 0.085 units. The linear Ridge regression attained the highest test R^2 (0.928, RMSE = 0.084), essentially matching the performance of more flexible tree ensembles such as ET ($R^2 = 0.927$) and SVR. This finding indicates that, once lagged inputs and the delta-prediction strategy are employed, the mapping from environmental variables to global thermal sensation is sufficiently approximated by linear relationships.

Local temperature predictions also showed distinct performance patterns. For Temperature near the ankle (T_{ankle}), all models achieved very high accuracy, with test R^2 values between 0.96 and 0.97. The best performance was obtained using SVR ($R^2 = 0.969$, $RMSE = 0.318$℃), followed closely by EN and GBRT. This confirms that the short-term dynamics of lower-body temperature can be accurately predicted from boundary conditions and recent thermal history. Conversely, Temperature near the head (T_{head}) proved more challenging to predict, exhibiting lower though still satisfactory accuracy. The HGBR model achieved the best results ($R^2 = 0.812$, $RMSE = 1.36$℃), outperforming other ensembles and linear models which hovered in the R^2 range of 0.78–0.80. The reduced predictability at the head level is consistent with the complex, localized dynamics involved, such as air movement, convective plumes, and partial shading, which are only partially captured by the available global input features.

Overall, the combination of delta-prediction, lagged inputs, and time-series cross-validation yielded stable and physically consistent surrogates. All four targets exhibited high training and test R^2 scores with no significant evidence of overfitting. Even for the complex head temperature dynamics, the best model explained more than 80% of the variance on an independent two-day period. These validated models form the backbone for the subsequent analyses, where they are used to quantify the Sun Patch Impact Index (SPI) and identify local–global mismatches under high solar loads.

To further investigate the relatively larger prediction error for the head-level temperature, the test samples were stratified into three solar operating regimes based on the measured solar radiation G: no direct sun ($G \leq 100\,W/m^2$), moderate sun patch ($100 < G \leq 400\,W/m^2$), and strong sun patch ($G > 400\,W/m^2$). The head-level prediction error was found to be strongly regime-dependent. Under no-direct-sun conditions, the model yielded RMSE = 0.311 °C, MAE = 0.213 °C, and mean bias = -0.157 °C. Under moderate sun-patch conditions, these values increased to RMSE = 0.615 °C, MAE = 0.426 °C, and mean bias = 0.078 °C. Under strong sun-patch conditions, the error increased to about 2 °C, with MAE = 1.672 °C and mean bias = -0.134 °C. These results indicate that the larger overall discrepancy is mainly associated with transient high-radiation periods, especially strong sun-patch events, rather than with uniformly poor model performance across all operating conditions. Moreover, the mean bias remains small in all three regimes, indicating that the main issue is not a persistent systematic offset, but rather an increase in residual dispersion under rapidly changing solar-driven conditions. This behavior is physically consistent with the fact that head-level temperature is governed by more localized and rapidly varying mechanisms, including convective mixing, plume interaction around the upper body, transient shading and sun exposure, and localized radiative asymmetry, which are not fully represented by the available explanatory variables.

4. Results and discussion

4.1. Experimental results

To determine whether the observed increase in indoor air

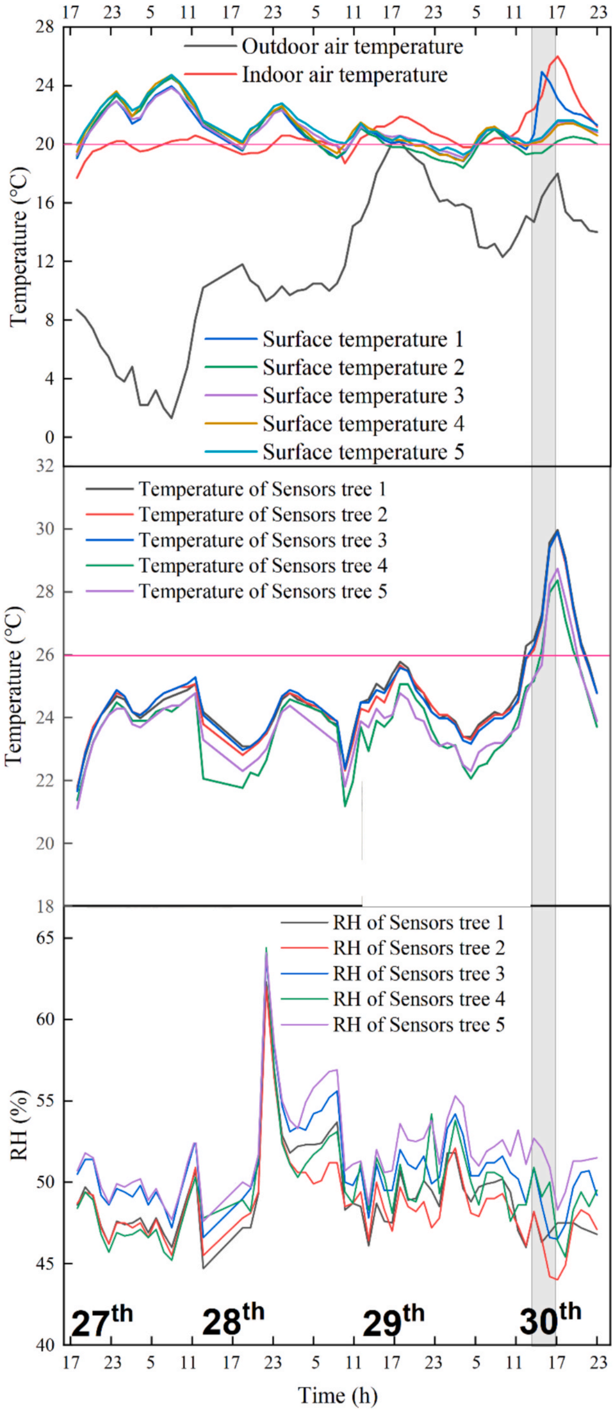

Fig. 5. Temporal profiles of indoor environmental parameters from 17:00 on 27 March to 00:00 on 30 March. The sun patch was present between 13:40 and 17:00 on 30 March.

temperature during the presence of a sun patch on the floor is attributable to outdoor environmental conditions or to the combined effect of direct solar radiation and outdoor temperature, the indoor environmental parameters corresponding to Scenario 1 (see Table 2) are analyzed and presented in Fig. 5. During the monitored period, the indoor air temperature reached a maximum of 26 °C. A comparison of outdoor air temperatures across two time intervals indicates that, between 13:40 and 17:00 on the 30th, the outdoor temperature was lower, whereas the indoor air temperature was higher. This divergence is associated with the presence of direct solar radiation, thereby indirectly demonstrating that the sun patch plays a dominant role in driving the indoor temperature increase.

During the sunshine period, the floor surface temperature at measurement point 1 (see Fig. 3) gradually increased, reaching a maximum value of 25.5 °C. Subsequently, the floor temperature decreased as a result of the westward movement of the sun. Compared with conditions at 14:20, the sun patch area on the right side of the manikin was reduced (at 15:00), leading to a smaller irradiated floor area and diminished direct solar radiation. Although the floor temperature began to decline, the indoor air temperature continued to rise due to buoyancy-driven natural convection, whereby heated air ascended within the space. Consequently, the indoor air temperature reached its peak shortly after the sun patch had disappeared.

In addition, the air temperature measured at a height of 1.68 m exhibited a trend similar to that of the indoor air temperature during the presence of the sun patch. Both temperatures reached their respective peaks shortly after the end of the solar exposure period, which can be attributed to the thermal inertia of the indoor environment. Concurrently, relative humidity decreased progressively as temperature increased, with more pronounced variations observed for sensor trees 1 and 2. This behavior can be explained by the increase in the saturation water vapor capacity of air at higher temperatures, resulting in lower relative humidity. Furthermore, radiant heating from the sun patch enhances the evaporation rate of moisture, leading to localized reductions in humidity.

Moreover, when the sun patch was present, the measured head temperature of the thermal manikin in the seated position exceeded the reference temperature at multiple test locations, with peak values surpassing 30 °C. This observation confirms that prolonged exposure to direct solar radiation can induce thermal discomfort. Although the PID-controlled floor heating system (FHS) operated with adequate accuracy, it lacked predictive capability with respect to the additional thermal input from the sun patch and was unable to account for floor surface temperature when relying on a constant air-temperature-based setpoint. These findings indicate potential for improving control strategies, such as lowering the setpoint within the thermal comfort range, implementing a climate-based adaptive setpoint profile, or incorporating continuous floor surface temperature monitoring while using the constant setpoint as a reference.

4.2. *Linear correlations and feature dependencies*

Fig. 6 illustrates the Pearson correlation coefficients between the input environmental features and the target thermal comfort variables. A preliminary analysis of the environmental features reveals strong interdependencies: outdoor (T_{out}) and operative (T_{op}) temperatures are tightly coupled ($r \approx 0.79$). Since the building envelope includes two large windows located in one façade, the U-value is lower making indoor environment highly correlated to outdoor climatic conditions. Both temperatures show a strong negative correlation with the mean inlet water temperature ($r \approx -0.90$ and -0.78, respectively), which captures the active regulation of the hydronic floor system (i.e., higher water temperatures are supplied as indoor and outdoor temperatures drop). Indoor relative humidity (*RH*) tends to inversely correlate with temperature, consistent with seasonal heating effects where higher indoor temperatures typically correspond to lower humidity levels.

Regarding the target variables, BAC exhibits only weak linear associations with any single environmental feature (r ranging from -0.18 to $+\ 0.21$). The modest correlation with direct solar radiation ($r \approx 0.1$) suggests that sun patch is a coarse proxy for the precise radiant asymmetry experienced by the occupant. This lack of strong linear predictors underscores that overall comfort is a derivative of non-linear interactions among mean radiant temperature, vertical gradients, and the thermal inertia of the building. These findings support the modeling results in Section 3.3, where non-linear ensemble methods (Random Forest) outperformed linear baselines for predicting BAC.

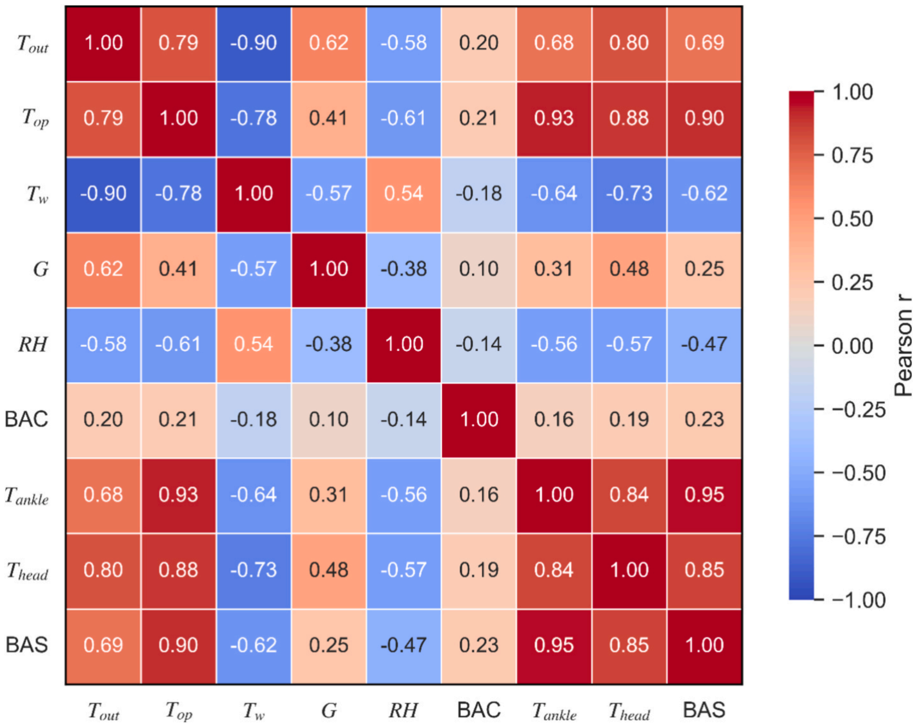

	T_{out}	T_{op}	T_w	G	RH	BAC	T_{ankle}	T_{head}	BAS
T_{out}	1.00	0.79	-0.90	0.62	-0.58	0.20	0.68	0.80	0.69
T_{op}	0.79	1.00	-0.78	0.41	-0.61	0.21	0.93	0.88	0.90
T_w	-0.90	-0.78	1.00	-0.57	0.54	-0.18	-0.64	-0.73	-0.62
G	0.62	0.41	-0.57	1.00	-0.38	0.10	0.31	0.48	0.25
RH	-0.58	-0.61	0.54	-0.38	1.00	-0.14	-0.56	-0.57	-0.47
BAC	0.20	0.21	-0.18	0.10	-0.14	1.00	0.16	0.19	0.23
T_{ankle}	0.68	0.93	-0.64	0.31	-0.56	0.16	1.00	0.84	0.95
T_{head}	0.80	0.88	-0.73	0.48	-0.57	0.19	0.84	1.00	0.85
BAS	0.69	0.90	-0.62	0.25	-0.47	0.23	0.95	0.85	1.00

Fig. 6. Pearson correlation heatmap illustrating the linear dependencies between environmental input features and the target thermal comfort variables.

In sharp contrast, BAS demonstrates a much stronger linear dependence on the thermal state. BAS correlates very highly with operative temperature ($r \approx 0.9$) and strongly with outdoor air temperature ($r \approx 0.69$). This sensitivity indicates that perceived warmth is largely driven by the mean thermal environment rather than complex gradients. The moderate positive link with solar radiation ($r \approx 0.25$) confirms that sun patches contribute to perceived warmth, though they are secondary to the dominant air temperature. The high linearity of BAS explains the excellent performance of the Ridge regression model observed in Table 3.

The analysis of local temperatures reveals distinct vertical dynamics. Ankle-level temperature (T_{ankle}) is almost perfectly aligned with the operative temperature ($r \approx 0.93$) and shows a modest correlation with solar radiation ($r \approx 0.31$). This suggests that near-floor conditions are governed primarily by the bulk indoor air and the floor surface temperature, with solar gains playing a secondary role. Conversely, Head-level temperature (T_{head}), while still tracking operative temperature ($r \approx 0.88$), exhibits a significantly stronger correlation with solar radiation ($r \approx 0.48$). This distinction implies that sun patches combined with the temperature stratification have a more pronounced direct effect on the upper body (further discussed in the next section), likely due to direct radiant exposure through the façade. This increased sensitivity to transient solar loads aligns with the finding that head temperature is the most challenging variable to predict, requiring models that can capture rapid radiative dynamics.

4.3. Non-linearities and regime-dependent relationships

Fig. 7 presents the pairwise relationships between the temperature near the head (T_{head}) and the environmental input features. While the correlation analysis in Fig. 6 quantified linear associations, this visual inspection reveals complex, non-linear dependencies and regime-specific behaviors that are critical for accurate modeling. The scatter plots indicate that T_{head} is most tightly coupled with the indoor operative temperature (T_{op}), forming a narrow, near-linear band. This confirms that the local thermal state is predominantly governed by the global indoor environment.

In contrast, the relationship with outdoor air temperature (T_{out}) is broader and curvilinear, illustrating how the building envelope and thermal mass filter the external climate signal before it affects the occupant. Significant dynamic effects are observable in the relationship with the mean inlet water temperature (T_w). The data forms distinct hysteresis-like loops rather than a single functional curve. This pattern is consistent with the thermal inertia of the hydronic floor system, where the system's trajectory differs during ramp-up (heating) versus cool-down phases. Similarly, the interaction with direct solar radiation (G) displays marked heteroscedasticity and saturation effects; while T_{head} generally rises with irradiance, the wide dispersion reflects the intermittent nature of sun patches and variable occupant exposure, which cannot be captured by a simple linear coefficient. Finally, the diagonal histograms highlight the multimodal distribution of several drivers, particularly solar radiation (heavily right-skewed) and relative humidity (clustered mid-range). The resulting clustered shapes in the off-diagonal plots suggest distinct operating regimes (e.g., active heating vs. free-running periods). These structural complexities, specifically the hysteresis, non-linearity, and regime shifts, underscore the necessity of the proposed surrogate modeling approach. A simple static regression would fail to capture these dynamics, whereas the delta-prediction strategy, enriched with lagged inputs, is specifically designed to resolve these transient responses to moving solar loads and system adjustments.

4.4. Time-series reconstruction and dynamic response

Fig. 8 presents the time-series reconstruction of the four thermal-comfort related variables over the independent test period, comparing the observed values against the one-step-ahead predictions generated by the best-performing model for each target. The results validate the efficacy of the delta-prediction strategy, as the models successfully capture both the broad diurnal trends and specific transient events.

Regarding the global comfort indices, the Random Forest model for BAC closely tracks the full diurnal evolution, accurately reproducing the sharp rise and peak magnitude observed around 19:00 on April 8th. While there are occasional underestimation during the steepest ramp-up

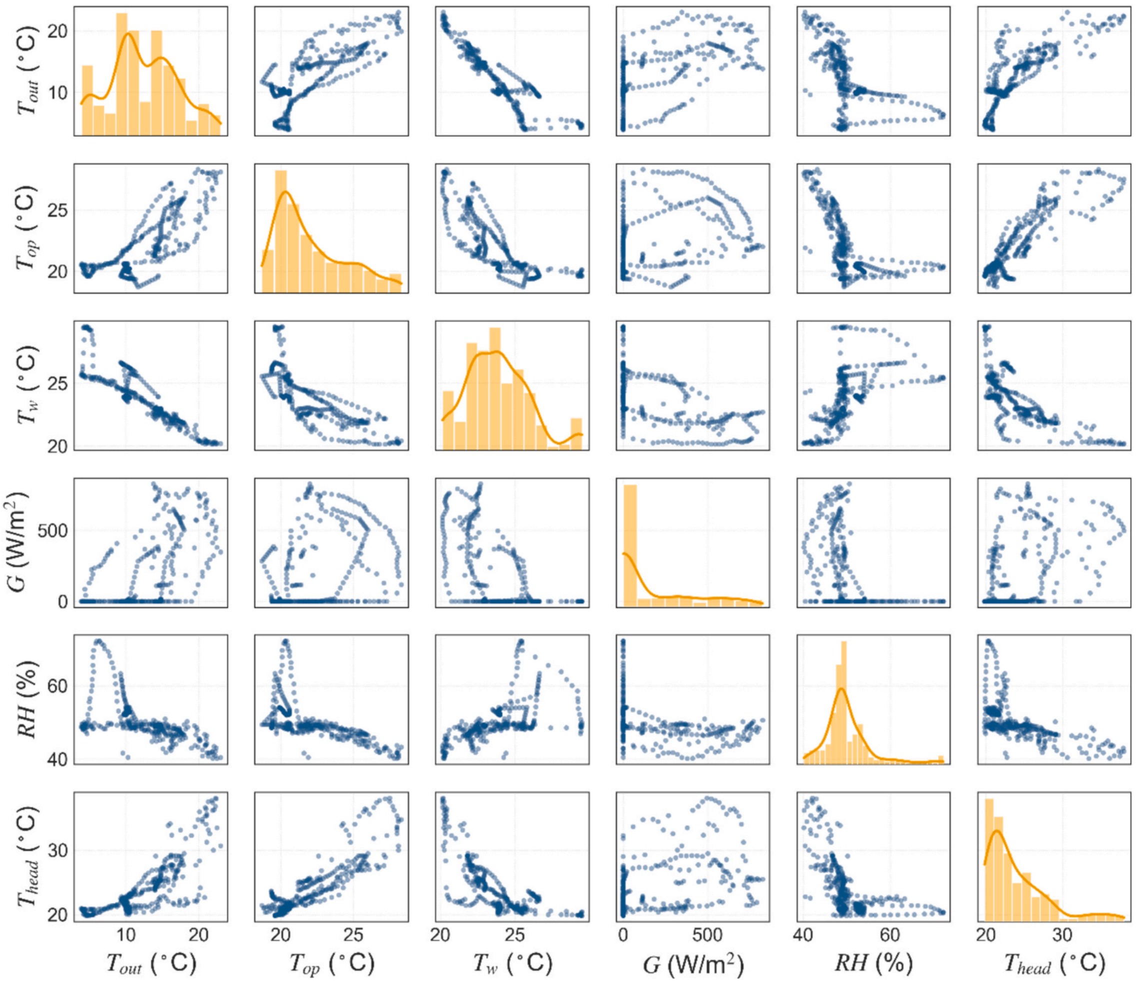

Fig. 7. Pairwise scatter plot matrix illustrating the non-linear relationships and distributions between environmental input features and the temperature near the head. The diagonal panels display the univariate kernel density estimation (KDE) for each variable, highlighting data distribution and multimodality..

events, the model effectively captures the non-linear volatility of the comfort vote. Conversely, the BAS predictions, generated by Ridge regression, exhibit a smooth trajectory that aligns almost parallel to the observed data. This behavior confirms the predominantly linear dependence of thermal sensation on the recent thermal state (specifically operative temperature), yielding faithful plateaus and gentle decay phases, albeit with a slight smoothing of high-frequency fluctuations during rapid transitions. The local temperature predictions highlight the models' ability to distinguish between inertia-driven and radiation-driven dynamics. For the temperature near the ankle (T_{ankle}), the SVR (RBF) model accurately captures the smooth, high inertia warming and cooling cycles. It reproduces the peak thermal load near 18:00–19:00 and the subsequent decay with high fidelity, effectively filtering out measurement noise while maintaining the structural trend. In contrast, the temperature near the head (T_{head}) exhibits much more volatile dynamics due to direct sun-patch exposure. The HGBR successfully reproduces these abrupt jumps, specifically the sharp rise preceding 16:30 and the immediate drop thereafter, while maintaining tight alignment during the extended evening cool-down. Collectively, these traces demonstrate that learning the rate of change (Δy) rather than the absolute value effectively disentangles thermal persistence from external forcing. The models successfully capture short-horizon dynamics driven by moving solar patches and radiant system adjustments. The remaining residual errors are primarily characterized by brief phase lags and mild peak clipping during rapid transients, which are expected physical limitations given the thermal mass of the building and the control hysteresis of the hydronic system.

The observed and predicted vertical air temperature difference ($T_{head} - T_{ankle}$) systematically reveals a pronounced vertical temperature stratification during the monitored period. At peak conditions, ankle temperatures rise to approximately 28 °C, while head temperatures exceed 34 °C, resulting in a vertical gradient far greater than the 3 °C per meter limit recommended by ISO 7730 and ASHRAE 55 for seated occupants. This excessive gradient indicates a strong non-uniformity in thermal exposure, which can significantly impact occupant comfort and physiological responses. Elevated head temperatures combined with relatively cooler ankle conditions may lead to localized discomfort, thermal stress, and potential dissatisfaction.

It is worth noting that, while the thermal manikin monitors 34 independently controlled zones capable of capturing detailed skin temperature distributions, this study prioritizes the vertical axis (head and ankle level) as the primary target for surrogate modeling. This choice is driven by the specific thermal dynamics of hydronic floor systems, where the interaction between the heated slab and direct sun patches creates extreme vertical stratification. However, the manikin's orientation facing the glazing means it simultaneously experiences significant radiant temperature asymmetry between its irradiated front and shaded back segments. One limitation of this work is that while this study identifies vertical local–global mismatches, it does not explicitly model the radiant asymmetry between the irradiated front and shaded back of the manikin. Given that the manikin was seated facing the glazing, directional skin temperature differences are a primary factor in solar-induced discomfort. Future work should exploit the full 34-zone skin temperature dataset to develop surrogates for lateral asymmetry

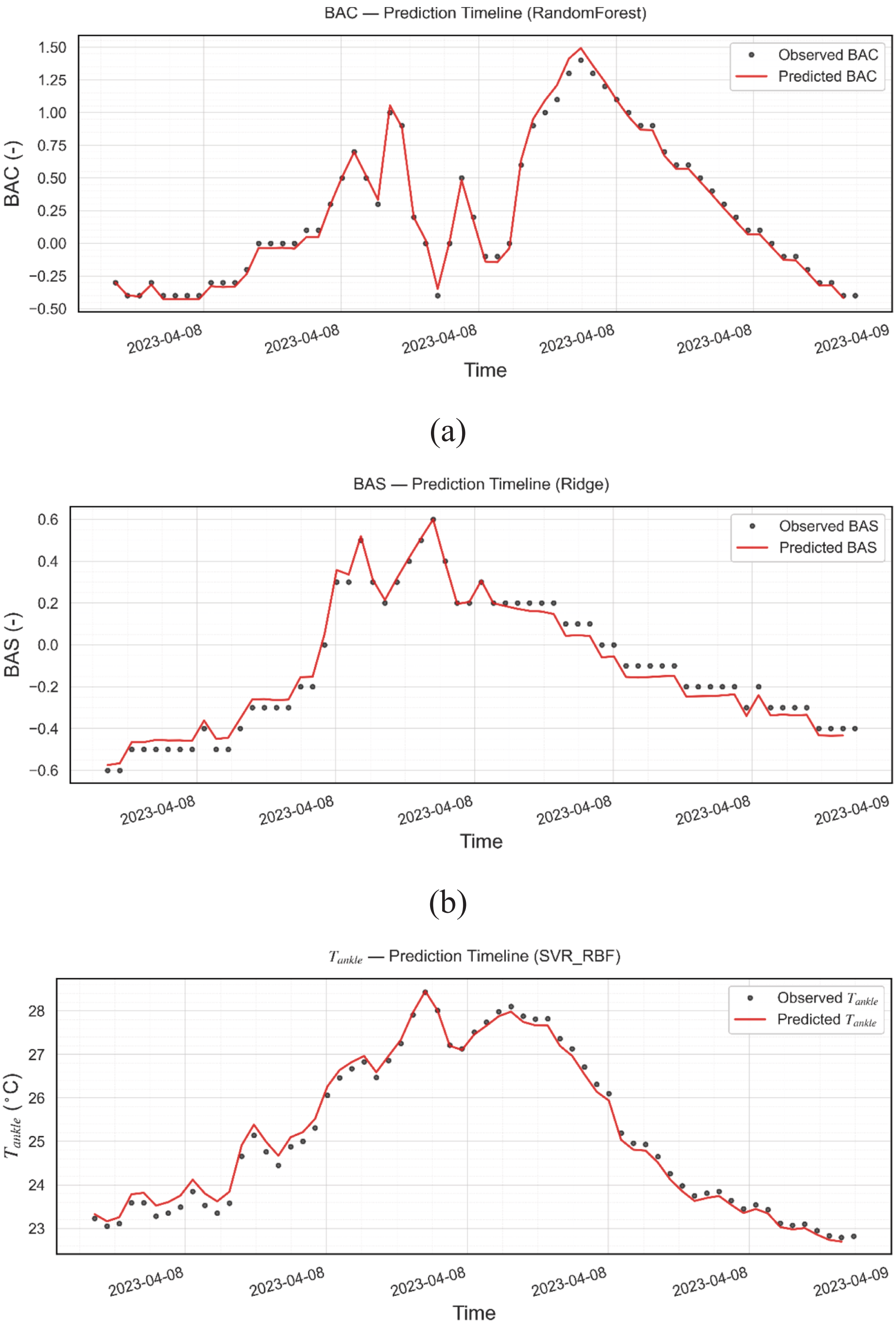

(a)

(b)

(c)

Fig. 8. Time-series comparison of observed and predicted values for the four thermal comfort targets during the independent test period. The predictions represent the best-performing model for each variable: (a) BAC using Random Forest; (b) BAS using Ridge Regression; (c) T_{ankle} using SVR-RBF; (d) T_{head} using HGBR; and (e) vertical air temperature difference ($T_{head} - T_{ankle}$).

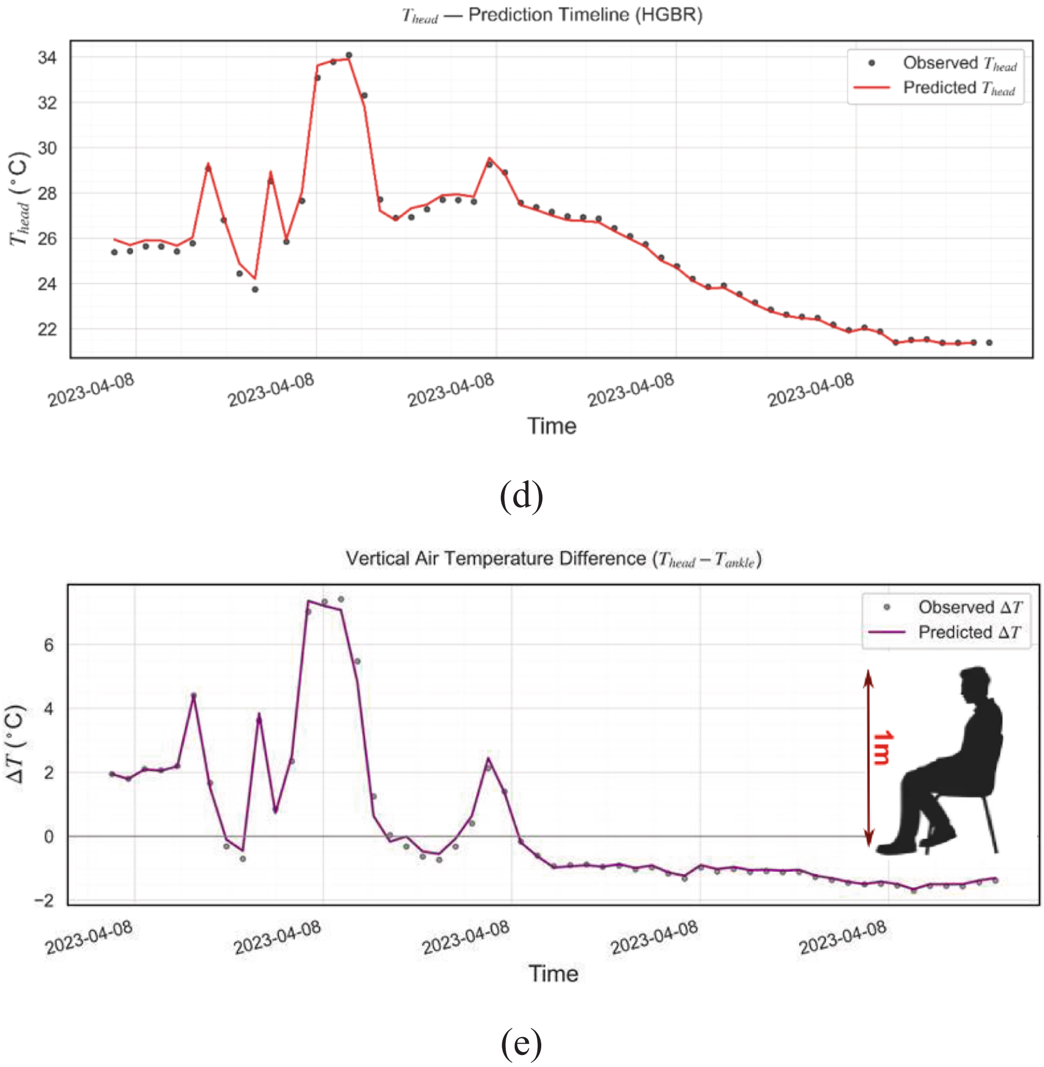

(d)

(e)

Fig. 8. (*continued*).

indices. This would allow for a more granular 'local–global' diagnostic that accounts for both the floor-driven vertical gradients and the window-driven directional radiation

4.5. *Physical interpretability via SHAP analysis*

To elucidate how the machine learning models exploit boundary conditions and indoor states, a SHAP (SHapley Additive exPlanations) analysis was performed on the GBRT-Huber models. Given the use of lagged inputs, individual SHAP values were aggregated back onto the five primary physical drivers: T_{out}, T_w, direct solar radiation (G), T_{op}, and RH. Fig. 9 visualizes the distribution of these contributions as summary dot plots, while Table 4 reports the mean absolute grouped SHAP values, ranking the drivers by their marginal contribution to the prediction.

For the BAC, Table 4 shows that the indoor operative temperature is the primary driver (mean $|\text{SHAP}| \approx 0.0129$). This reflects the direct dependence of the overall comfort vote on the room's global thermal state. However, this is closely followed by the inlet water temperature ($T_w \approx 0.0107$) and relative humidity ($RH \approx 0.0105$). As illustrated in Fig. 9a, the impact of RH is highly significant, indicating that global comfort is a composite phenomenon where the operative temperature sets the baseline, while system regulation and moisture content act as critical modulators. Notably, G exerts the lowest influence (≈ 0.0041) on this global metric, suggesting that while sun patches cause local thermal asymmetry, their impact on the scalar comfort vote is indirect and buffered by the room's thermal inertia.

In sharp contrast to global comfort, the local temperature dynamics (T_{ankle} and T_{head}) are dominated by direct solar radiation. As shown in Table 4, G is the overwhelming explanatory variable for both ankle and head regions, with mean contributions of 0.0791 and 0.0802, respectively. The corresponding plots in Fig. 9c and Fig. 9d confirm this dominance, displaying a wide spread of SHAP values for G (blue-to-red distribution), which quantitatively validates the sun patch as the principal disturbance driving localized heating. The secondary drivers reveal important vertical distinctions. At head height (Fig. 9c), the operative temperature plays a robust secondary role (0.0611), indicating that the upper body is strongly coupled to the ambient room environment alongside the direct solar load. Conversely, at the ankle level (Fig. 9d), the influence of non-solar drivers is more diffuse; outdoor temperature, operative temperature, and humidity contribute roughly equally (≈ 0.021–0.026). This suggests that near-floor conditions are a complex interplay of external forcing, floor thermal mass, and solar gains, without a single dominant secondary driver.

For thermal sensation (BAS), the hierarchy of importance in Table 4 represents a hybrid between the local and global regimes. Direct solar radiation returns as the top driver (0.0093), confirming that occupants actively sense the transient warmth of sun patches. However, unlike the local temperature models, the contributions of operative temperature

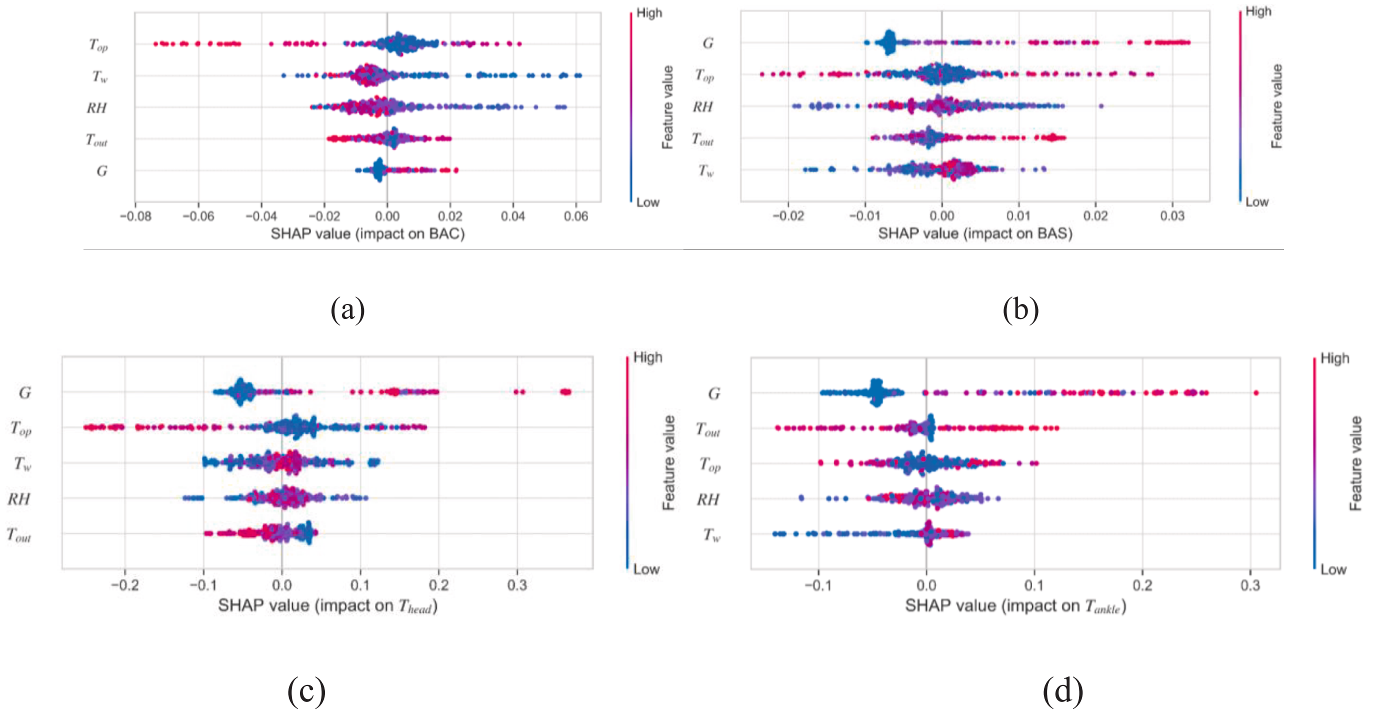

(a)

(b)

(c)

(d)

Fig. 9. SHAP summary plots illustrating the feature importance for the four target variables: (a) BAC; (b) BAS; (c) T_{head}; and (d) T_{ankle}. The x-axis represents the SHAP value (impact on model output), while the color gradient indicates the magnitude of the feature value (Red = High, Blue = Low). Features are ordered by their mean absolute contribution to the prediction. (For interpretation of the references to colour in this figure legend, the reader is referred to the web version of this article.)

Table 4
Mean absolute grouped SHAP values for the GBRT-Huber models, ranked by importance for each target variable.

Driver	BAC	T_{ankle}	T_{head}	BAS
G	0.0041	0.0791	0.0802	0.0093
T_{op}	0.0129	0.0243	0.0611	0.0051
T_w	0.0107	0.0195	0.0340	0.0038
RH	0.0105	0.0211	0.0248	0.0050
T_{out}	0.0054	0.0264	0.0231	0.0038

(0.0051) and relative humidity (0.0050) are significant, accounting for roughly half the weight of solar radiation. The distribution in Fig. 9b supports this, showing that while high solar radiation (red dots) pushes sensation higher, the overall variance is tightly constrained by the bulk room conditions (T_{op} and RH). This implies that the BAS index acts as a low-pass filter, integrating rapid solar signals with slower inertial signals.

To complement the global-average SHAP results, a stratified grouped-SHAP analysis was performed using the same solar operating regimes introduced in Section 3.3. The regime dependence was found to be most pronounced for the local temperature responses. For the head-level temperature, the grouped SHAP importance of solar radiation G increased from 0.0519 under no-direct-sun conditions to 0.2259 under strong sun-patch conditions, corresponding to an increase from approximately 37% to 71% of the total grouped importance. For the ankle-level temperature, the grouped SHAP importance of G increased from 0.0447 to 0.1514, corresponding to an increase from about 41% to 73%. These results indicate that solar forcing becomes markedly more influential for the localized thermal response during direct sun exposure.

At the same time, under no-direct-sun conditions, the grouped SHAP contributions were much closer to one another, especially for the head-level temperature, where G remained the largest single contributor but was followed relatively closely by T_{out} and T_{op}. This more distributed pattern suggests that the model response in this regime is not governed by instantaneous direct solar forcing alone, but is also consistent with lagged solar influence, residual thermal-memory effects, and delayed surface and near-body air response. Therefore, although G still contributes under no-direct-sun conditions, its role is much less dominant than under strong sun-patch conditions.

For the whole-body outputs BAC and BAS, the stratified SHAP analysis showed a more distributed behavior across variables. In BAC, T_{op} was the leading contributor under no-direct-sun and moderate sun-patch conditions, with grouped SHAP values of 0.0278 and 0.0173, respectively, whereas under strong sun-patch conditions T_w became dominant (0.0175), with T_{op} and T_{out} contributing comparably (0.0104 each). In BAS, T_{op} was the leading contributor under no-direct-sun conditions (0.0104), while T_{out} became dominant under both moderate and strong sun-patch conditions, with grouped SHAP values of 0.0169 and 0.0200, respectively. This is physically consistent with the fact that BAC and BAS are integrated whole-body metrics, whereas the head- and ankle-level temperatures are more directly linked to localized solar-driven non-uniformity. Overall, the stratified grouped-SHAP analysis indicates that predictor importance is regime-dependent, but that this dependence is substantially stronger for the local temperatures than for the integrated comfort and sensation indices.

Overall, the grouped SHAP analysis provides a physically consistent interpretation of the learned model structures: (i) Global integration: global comfort (BAC) is governed primarily by the integrated room state, especially operative temperature, hydronic system output, and humidity; (ii) Local transient response: local temperatures are the outputs most strongly influenced by solar radiation, with the contribution of G increasing markedly under strong sun-patch conditions; and (iii) Hybrid sensation: thermal sensation (BAS) occupies an intermediate position, reflecting both solar gains and the background indoor thermal environment. These results justify the focus on direct solar radiation as the key perturbation variable for the subsequent Sun Patch Impact (SPI) analysis.

5. Sun patch impact index (SPI): Model-based counterfactual analysis

Following the selection of the best-performing one-step-ahead models (Section 3.3), we quantified the specific contribution of direct solar radiation to thermal comfort via a model-based counterfactual experiment. Let $\hat{y}_{with}(t+1)$ represent the predicted target value at time $t+1$ (whether body average sensation, comfort, or a local temperature) derived using the measured direct solar radiation $G(t)$ alongside all other environmental inputs. To isolate the effect of the sun patch, we constructed a counterfactual test set where the 'Direct solar radiation' feature is replaced by a baseline value $G_{base} = 0W/m^2$ ('without sun patch'), while all other variables, including outdoor temperature, indoor operative temperature, inlet water temperature, relative humidity, and lagged target values, are held constant. Using the same trained model, a secondary prediction $\hat{y}_{without}(t+1)$ is computed. The Sun Patch Impact Index (SPI) is defined at each time step as the difference between these two predictions:

$$SPI(t+1) = \hat{y}_{with}(t+1) - \hat{y}_{without}(t+1) \tag{7}$$

The SPI shares the units of the target variable (dimensionless for comfort/sensation indices, °C for local temperatures). A positive SPI indicates that the presence of the sun patch increases the predicted parameter relative to the theoretical 'without sun patch' baseline under identical ambient conditions. Fig. 10 presents the SPI analysis for BAS during the test period. As shown in the time-series comparison (Fig. 10a), the SPI remains strictly positive whenever $G > 0$, confirming that solar exposure systematically elevates the predicted sensation. The impact rises from approximately 0.02 units at low irradiance to peak values between 0.04 and 0.05 when direct solar radiation reaches 700–800 W/m^2. Notably, the peak SPI occurs slightly after the maximum solar irradiance and decays more gradually. This lag is consistent with the thermal inertia encoded in the model's input structure, reflecting the physical delay between radiative exposure and the physiological perception of warmth.

The statistical distribution of the impact is visualized in Fig. 10b. The

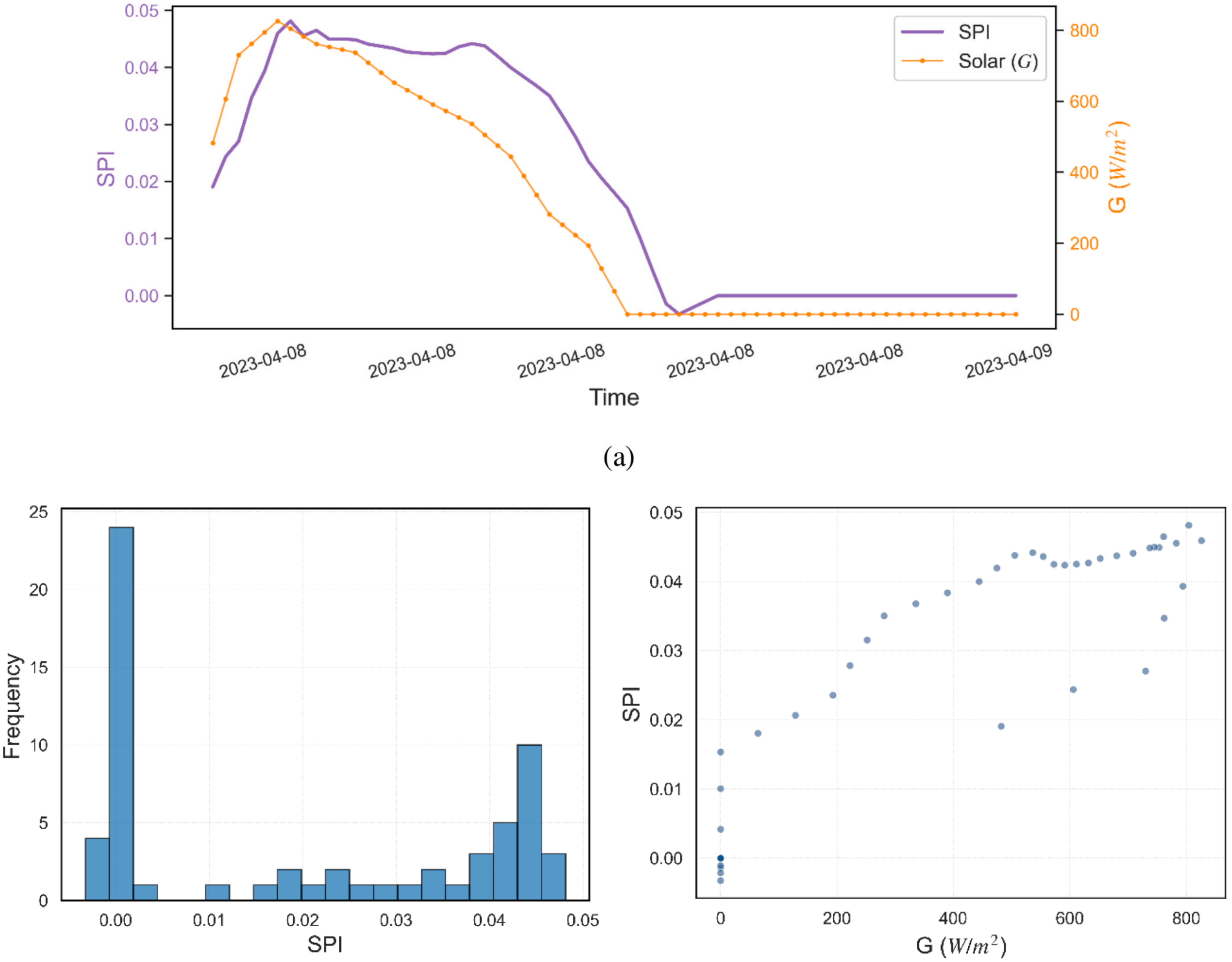

(a)

(b)

(c)

Fig. 10. Sun Patch Impact (SPI) analysis for BAS during the test period. (a) Time-series evolution of the calculated SPI (purple solid line, left axis) plotted against the measured direct solar radiation G (orange dotted line, right axis), showing the temporal lag between peak irradiance and peak sensation impact. (b) Histogram of SPI values, confirming a strictly positive, right-skewed distribution under solar exposure. (c) Scatter plot of SPI versus direct solar radiation, illustrating the non-linear saturation effect and hysteresis (state-dependent response) at high irradiance levels. (For interpretation of the references to colour in this figure legend, the reader is referred to the web version of this article.)

histogram confirms that the majority of non-zero SPI values cluster in the range of 0–0.05, with no negative tail, validating the model's stability (i.e., removing solar gains does not erroneously predict heating). The relationship between the impact and its driver is further detailed in the scatter plot (Fig. 10c), which reveals a clear monotonic trend. The SPI increases steeply at low-to-moderate irradiance levels ($G < 400W/m^2$) before exhibiting signs of saturation at high irradiance. In practical terms, eliminating the sun patch during peak hours would decrease the predicted sensation index by approximately 0.03–0.04 units (e.g., shifting a vote from -0.50 to -0.54). While modest in absolute terms over a single 10-minute horizon, this systematic shift represents a physically meaningful contribution to the overall thermal vote.

A critical feature observed in the scatter plot (Fig. 10c) is that the data points do not collapse onto a single, perfect curve; at intermediate and high irradiances, distinct branching is visible. This behavior is not a numerical artifact but rather a reflection of the dynamic, state-dependent response captured by the surrogate model. Because the predictor incorporates autoregressive lags, the marginal impact of a specific solar load is modulated by the recent thermal history. On the rising limb of the solar cycle, when the indoor environment is cooler, a given increase in radiation produces a larger change in sensation. Conversely, later in the afternoon, once the space has warmed and the hydronic system has responded, the same irradiance induces a smaller incremental shift. This hysteresis-like pattern captures the expected inertia of the building-plant-occupant system, demonstrating the model's ability to distinguish between transient exposure and steady-state conditions.

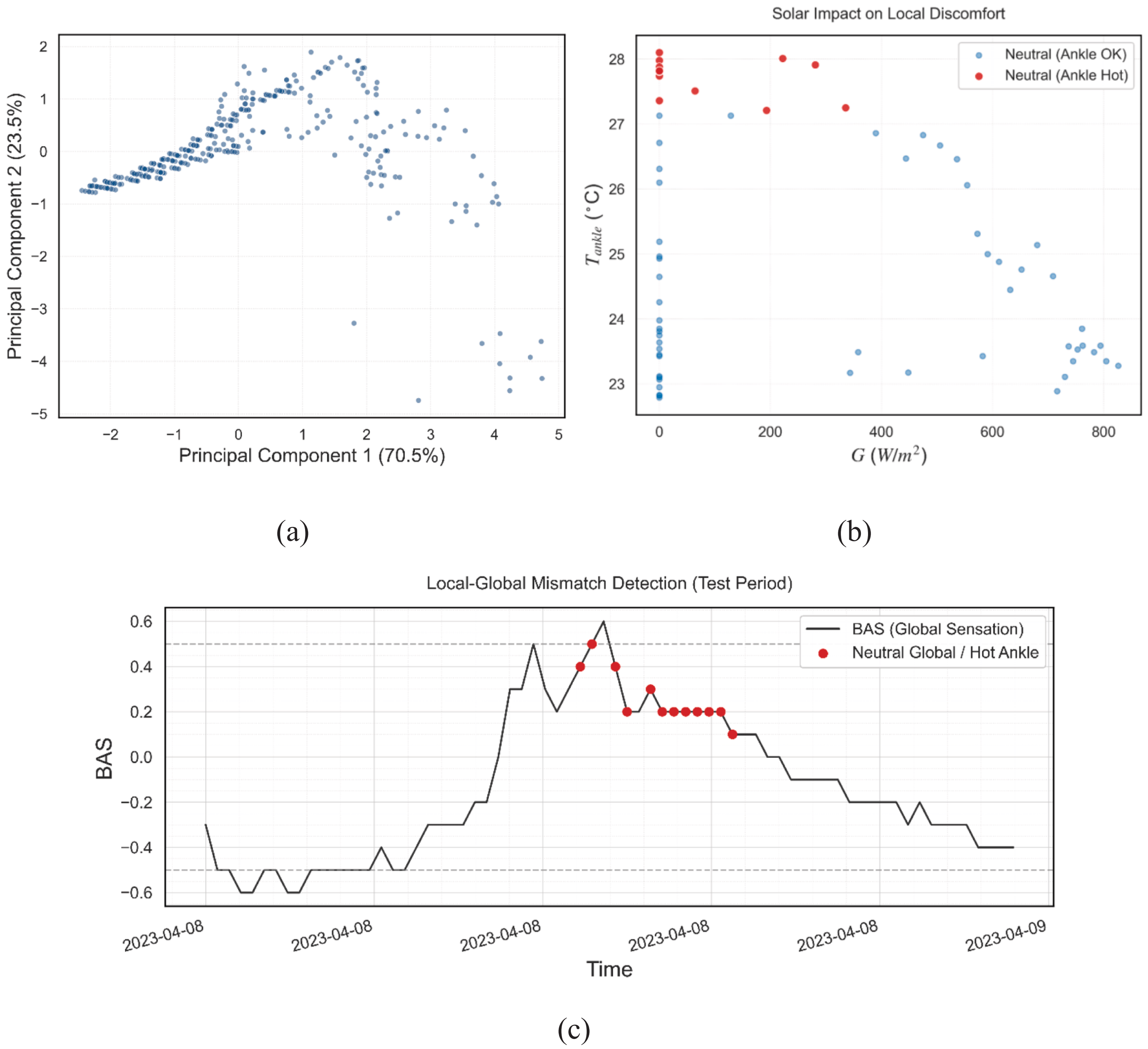

Fig. 11. Analysis of comfort modes and local–global mismatches. (a) PCA projection of the four thermal targets, revealing a dominant ‘Global Warmth’ mode (PC1) and an orthogonal ‘Subjective Comfort’ mode (PC2); (b) Scatter plot of Ankle Temperature vs. Solar Radiation for neutral sensation periods, showing that high ankle temperatures (red points) persist even as solar forcing diminishes, indicating thermal inertia effects; (c) Time-series of BAS on the test day, with red markers highlighting ‘hidden’ local discomfort events where BAS is neutral ($|\text{BAS}| \leq 0.5$) but ankle temperature is high ($>$ 80th percentile). (For interpretation of the references to colour in this figure legend, the reader is referred to the web version of this article.)

6. Comfort modes, local–global mismatch and behavioral adaptation

To investigate the redundancy and complementarity of the four thermal comfort-related outputs, a Principal Component Analysis (PCA) was performed on the standardized time series of Body Average Comfort, Body Average Sensation, and the local operative temperatures near the head and ankle. The dataset spanned both training and testing periods to capture the full range of variability. The first two principal components (PC1 and PC2) explain 70.5% and 23.5% of the total variance, respectively, cumulatively accounting for approximately 94%. This implies that the four-dimensional target space can be effectively reduced to a two-dimensional ‘comfort manifold’. The component loadings reveal distinct physical interpretations. PC1 acts as a ‘Global Warmth’ mode, characterized by strong positive loadings for Ankle Temperature (0.57), Head Temperature (0.55), and Body Average Sensation (0.58), while Body Average Comfort contributes only weakly (0.18). In contrast, PC2 is dominated by Body Average Comfort (loading $+$ 0.98), acting as an orthogonal ‘Subjective Comfort’ mode. This structure suggests that the primary driver of variance is the simultaneous heating or cooling of the body and environment (PC1), while a secondary, independent factor captures variations in perceived comfort that are decoupled from the pure thermal sensation. The scatter plot of PC2 versus PC1 (Fig. 11a) confirms this, showing trajectories confined to specific bands, reflecting distinct comfort responses to similar thermal states.

While this low-dimensional representation captures the bulk system behavior, it risks obscuring localized discomfort. To investigate this, we analyzed the test period for ‘local–global mismatches’ −instances where the global sensation index indicates neutrality, yet local temperatures exceed recommended limits. We defined a ‘neutral zone’ for Body Average Sensation as $|\text{BAS}| \leq 0.5$, which encompasses 65 of the 70 test observations. Local overheating was identified using the 80th percentile thresholds for the test day: 27.13 ℃ for the ankle and 27.42 ℃ for the head. Within the globally neutral subset, we detected 12 instances of ‘hot ankle’ and 13 instances of ‘hot head’, meaning approximately 18–20% of nominally comfortable states actually masked local overheating risks. This phenomenon is critical for radiant floor systems, where excessive surface temperatures can cause foot discomfort, a risk explicitly addressed by ASHRAE 55 and ISO 7730 standards (which typically recommend floor temperatures stay below 29 ℃). Fig. 11c highlights these mismatch events on the BAS time series. The red markers indicate that ‘neutral but hot ankle’ events predominantly occur in the late afternoon. This timing is physically significant: it corresponds to the phase where the sun patch has shifted or faded, causing the whole-body sensation to relax toward neutral, while the high thermal mass of the floor retains heat, keeping ankle temperatures elevated.

This dynamic decoupling is further illustrated in Fig. 11b, which plots ankle temperature against direct solar radiation for neutral-sensation periods. The mismatch points cluster at the upper range of ankle temperatures but occur across a range of solar intensities, including low irradiance. This confirms a hysteretic lag between the instantaneous radiant load and the local thermal response. The ankle region remains warm well after the direct solar forcing has ceased, creating a residual local discomfort that the global sensation index fails to capture.

While this study relies on a static hypothesis by utilizing a seated thermal manikin to maintain experimental repeatability, it is acknowledged that human occupants in dynamic thermal environments are rarely stationary. In practice, exposure to direct solar radiation often triggers adaptive behaviors, such as adjusting body posture or utilizing shading devices (e.g., curtains), which can occur within the 10-minute horizon examined here. By maintaining a static subject, this research establishes a worst-case baseline for solar-induced thermal stress without the interference of behavioral mitigation. The finding that 20% of nominally 'neutral' global states actually mask local overheating risks at the ankle level is particularly significant in this context. It suggests that these “hidden” local discomfort events are the likely physical triggers for the very adaptive behaviors the reviewer mentions. Future iterations of this framework should integrate adaptive comfort models and occupant-shading interaction loops to transition from predicting unmitigated discomfort to adaptive comfort maintenance in high-performance glazed spaces.

7. Conclusion, work limitations and perspectives

This study presented a data-driven framework for modeling the short-term dynamics of global and local thermal comfort in spaces subjected to transient solar loads. By leveraging a ‘delta-prediction’ strategy, we developed surrogate models capable of forecasting the 10-minute evolution of occupant comfort with high fidelity, effectively disentangling the effects of active hydronic conditioning from the passive disturbance of moving sun patches. The results demonstrate that machine learning surrogates can accurately capture the non-linear thermal response of the room-occupant system. The best-performing models, specifically Random Forest for Body Average Comfort and Ridge Regression for Body Average Sensation, achieved high generalization capabilities (R^2 between 0.85 and 0.93) on independent test data. Notably, the local temperature near the ankle proved highly predictable ($R^2 \approx 0.97$), whereas the temperature near the head exhibited higher volatility ($R^2 \approx 0.81$), reflecting the complex convective and radiative interactions at the upper body level. Beyond predictive accuracy, the integration of explainable AI tools (SHAP) and counterfactual analysis (SPI) provided critical physical insights into the comfort drivers. We established that while global comfort is an integrated metric driven largely by operative temperature and humidity, local thermal risks are unequivocally dominated by direct solar radiation. The proposed Sun Patch Impact (SPI) index quantified this effect, showing that direct solar exposure systematically elevates thermal sensation by up to 0.05 scale units, with a clear hysteretic response dependent on the room's thermal history. From a practical control perspective, the identification of ‘local–global mismatches’ is a significant finding. Our analysis revealed that approximately 20% of the periods classified as ‘neutral’ by global sensation indices actually concealed local overheating risks at the ankle level. This decoupling, driven by the differing thermal inertia of the floor slab versus the air volume, suggests that standard thermostat-based feedback is insufficient for sun-exposed zones. Consequently, future predictive control strategies for radiant systems must explicitly incorporate local discomfort constraints and solar-aware feedforward logic to ensure true multi-objective comfort.

While the proposed machine learning framework demonstrated strong predictive performance and interpretability, several limitations warrant discussion. First, although the experimental dataset was collected under real climate conditions (non-controlled climatic scenarios), measurements may not fully capture the transient movement of occupants. Second, the surrogate models were trained on short-term horizons (10 min) over two to three days, which limits their applicability for long-term predictive control strategies without additional temporal scaling or hierarchical modeling. Third, the feature set relied primarily on global environmental variables and lagged states; localized radiative flux measurements and airflow data were not included, potentially constraining the accuracy of head-level temperature predictions where convective and radiant asymmetries dominate. Additionally, the thermal manikin approach, while providing high-resolution local comfort data, does not account for physiological adaptation mechanisms such as sweating or age adjustments, which could influence real occupant responses.

Future research should address these gaps by extending the modeling framework to multi-zone and naturally ventilated spaces, incorporating high-resolution radiant mapping and airflow sensors to better capture local dynamics. Integrating adaptive comfort models and physiological feedback loops could enhance realism and broaden applicability to diverse occupant profiles. Finally, from a control perspective, coupling the surrogate models with predictive optimization algorithms offers a promising avenue for solar-aware, multi-objective heating strategies that balance energy efficiency with local and global comfort constraints.

CRediT authorship contribution statement

Reda Snaiki: Writing – review & editing, Writing – original draft, Visualization, Validation, Software, Methodology, Investigation, Formal analysis, Conceptualization. **Abdelatif Merabtine:** Writing – review & editing, Writing – original draft, Supervision, Methodology, Investigation, Formal analysis, Data curation, Conceptualization. **Shengqiang Shi:** Writing – review & editing, Writing – original draft, Validation, Resources, Investigation, Formal analysis, Data curation. **Ines Grabaa:** Software, Investigation, Formal analysis.

Declaration of competing interest

The authors declare that they have no known competing financial interests or personal relationships that could have appeared to influence the work reported in this paper.

Data availability

Data will be made available on request.

References

[1] M.D.E. Sarmouk, A. Merabtine, A. Kheiri, S. Mokraoui, On the mitigation of the overheating caused by floor heating systems exposed to long direct solar radiation and high occupation rates, Sol. Energy 274 (2024), https://doi.org/10.1016/j.solener.2024.112565.

[2] Z. Kang, R. Tan, Q. Yao, J. Zhang, S. Zhang, Y. Wei, Numerical simulation of energy storage radiant floor heating systems with phase change materials having different thermophysical properties, Constr. Build. Mater. 463 (2025), https://doi.org/10.1016/j.conbuildmat.2025.140010.

[3] J. Hill, A. Athienitis, G. Larochelle-Marti, Methodology for design and predictive control of zones with STPV windows, motorized venetian blinds, and hydronic floor heating for net-zero energy buildings, In (2023) 590–597. https://www.scopus.com/inward/record.uri?eid=2-s2.0-85171187362&partnerID=40&md5=3b6eae9406018c3d410d62c504fafcfc.

[4] S. Shi, A. Merabtine, R. Bennacer, Radiant systems and solar-driven overheating: a comprehensive literature analysis over a decade, Build. Environ. 259 (2024), https://doi.org/10.1016/j.buildenv.2024.111659.

[5] Y. Du, C. Qian, X. Fu, The combined operating of radiant floor and fresh air coil in field experiment, in: 2014: pp. 741–755. https://doi.org/10.1007/978-3-642-39581-9_73.

[6] X. Zhou, Y. Liu, M. Luo, L. Zhang, Q. Zhang, X. Zhang, Thermal comfort under radiant asymmetries of floor cooling system in 2 h and 8 h exposure durations, Energ. Buildings 188–189 (2019) 98–110, https://doi.org/10.1016/j.enbuild.2019.02.009.

[7] ISO 7730:2005 Ergonomics of the thermal environment—PMV/PPD indices and local thermal comfort criteria., (2005).

[8] Standard 55-2023 – Thermal Environmental Conditions for Human Occupancy, (2023).

[9] R.F. Rupp, J. Kim, J. Toftum, G. Brager, R. de Dear, Ten questions concerning the application of adaptive thermal comfort in mixed-mode buildings, Build. Environ. 284 (2025) 113490, https://doi.org/10.1016/j.buildenv.2025.113490.

[10] Y. Cheng, J. Niu, N. Gao, Thermal comfort models: a review and numerical investigation, Build. Environ. 47 (2012) 13–22, https://doi.org/10.1016/j.buildenv.2011.05.011.

[11] C. Marino, P. Misiani, A. Nucara, M. Pietrafesa, The effect of the climatic condition on the radiant asymmetry, Int. J. Heat Technol. 35 (2017) S419–S426. https://doi.org/10.18280/ijht.35Sp0157.

[12] S. Shi, A. Merabtine, R. Bennacer, J. Kauffmann, Experimental evaluation of the impact of real sun patch on radiant floor heating in highly glazed spaces, Build. Environ. 244 (2023), https://doi.org/10.1016/j.buildenv.2023.110799.

[13] T. Li, A. Merabtine, M. Lachi, R. Bennacer, J. Kauffmann, Experimental study on the effects of a moving sun patch on heating radiant slabs: the issue of occupants' thermal comfort, Sol. Energy 255 (2023) 36–49, https://doi.org/10.1016/j.solener.2023.03.028.

[14] W. Sun, Y. Zhang, Z. Ling, X. Fang, Z. Zhang, Experimental investigation on the thermal performance of double-layer PCM radiant floor system containing two types of inorganic composite PCMs, Energ. Buildings 211 (2020), https://doi.org/10.1016/j.enbuild.2020.109806.

[15] T. Li, A. Merabtine, M. Lachi, N. Martaj, R. Bennacer, Experimental study on the thermal comfort in the room equipped with a radiant floor heating system exposed to direct solar radiation, Energy 230 (2021), https://doi.org/10.1016/j.energy.2021.120800.

[16] M.-H. Benzaama, M. Lachi, C. Maalouf, A.-M. Mokhtari, G. Polidori, M. Makhlouf, Study of the effect of sun patch on the transient thermal behaviour of a heating floor in Algeria, Energ. Buildings 133 (2016) 257–270, https://doi.org/10.1016/j.enbuild.2016.09.066.

[17] Q. Dong, S. Li, C. Han, Numerical and experimental study of the effect of solar radiation on thermal comfort in a radiant heating system, J. Build. Eng. 32 (2020) 101497, https://doi.org/10.1016/j.jobe.2020.101497.

[18] R.-L. Hwang, P.-L. Fang, W.-A. Chen, Impact of solar radiation on indoor thermal comfort near highly glazed façades in a hot-humid subtropical climate: an experimental evaluation, Build. Environ. 243 (2023) 110725, https://doi.org/10.1016/j.buildenv.2023.110725.

[19] Z. Qavidel Fard, Z.S. Zomorodian, S.S. Korsavi, Application of machine learning in thermal comfort studies: a review of methods, performance and challenges, Energ. Buildings 256 (2022), https://doi.org/10.1016/j.enbuild.2021.111771.

[20] A.B. Dhanushkodi, D. Kannamma, Enhancing Tmrt Predictions with Machine Learning: Combining Field Data and ENVI-Met Simulations, in: 2025: pp. 113–120. https://doi.org/10.1007/978-981-95-1442-7_10.

[21] T.M.S. Kumar, C.P. Kurian, Real-time data based thermal comfort prediction leading to temperature setpoint control, J. Ambient Intell. Hum. Comput. 14 (2023) 12049–12060, https://doi.org/10.1007/s12652-022-03754-8.

[22] A. Dogan, N. Kayaci, A. Bacak, Machine learning-based predictive model for temperature and comfort parameters in indoor enviroment using experimantal data, Appl. Therm. Eng. 259 (2025), https://doi.org/10.1016/j.applthermaleng.2024.124852.

[23] N. Alam, S.A. Zaki, S.A. Ahmad, M.K. Singh, A. Azizan, N. Othman, Machine learning approach for predicting personal thermal comfort in air conditioning offices in Malaysia, Build. Environ. 266 (2024), https://doi.org/10.1016/j.buildenv.2024.112083.

[24] X. Zhou, L. Xu, J. Zhang, B. Niu, M. Luo, G. Zhou, X. Zhang, Data-driven thermal comfort model via support vector machine algorithms: Insights from ASHRAE RP-884 database, Energ. Buildings 211 (2020), https://doi.org/10.1016/j.enbuild.2020.109795.

[25] R. Guo, B. Yang, Y. Guo, H. Li, Z. Li, B. Zhou, B. Hong, F. Wang, Machine learning-based prediction of outdoor thermal comfort: Combining Bayesian optimization and the SHAP model, Build. Environ. 254 (2024), https://doi.org/10.1016/j.buildenv.2024.111301.

[26] O.A. Al-Sharif, A.E. Newir, M.A. Halawa, Predicting thermal preferences-a comparative analysis of machine learning algorithms using ASHRAE global thermal comfort database II, J. Adv. Res. Fluid Mech. Therm. Sci. 115 (2024) 50–60. https://doi.org/10.37934/arfmts.115.2.5060.

[27] A. Rahmanparast, M. Milani, M. Camci, Y. Karakoyun, A.S. Dalkilic, Parameter reduction for PMV prediction via data driven approaches using the ASHRAE global thermal comfort database II and chinese dataset, Appl. Therm. Eng. 279 (2025), https://doi.org/10.1016/j.applthermaleng.2025.127553.

[28] R. Wang, S. Lu, W. Feng, A novel improved model for building energy consumption prediction based on model integration, Appl. Energy 262 (2020), https://doi.org/10.1016/j.apenergy.2020.114561.

[29] S. Yang, M.P. Wan, W. Chen, B.F. Ng, S. Dubey, Model predictive control with adaptive machine-learning-based model for building energy efficiency and comfort optimization, Appl. Energy 271 (2020), https://doi.org/10.1016/j.apenergy.2020.115147.

[30] N. He, J. Guo, Y. Li, Y. Quan, R. Li, L. Yang, Stochastic model predictive control for the optimal operation of office buildings, Build. Environ. 267 (2025), https://doi.org/10.1016/j.buildenv.2024.112248.

[31] J. Zhao, L. Shi, J. Li, H. Li, Q. Han, A model predictive control regulation model for radiant air conditioning system based on delay time, Journal of Building Engineering 62 (2022), https://doi.org/10.1016/j.jobe.2022.105343.

[32] S. Lu, M. Cui, B. Gao, J. Liu, J. Ni, J. Liu, S. Zhou, A Comparative Analysis of Machine Learning Algorithms in predicting the Performance of a combined Radiant Floor and Fan Coil Cooling System, Buildings 14 (2024), https://doi.org/10.3390/buildings14061659.

[33] H.S. Xie, S.R. Gandla, M. Bhattacharya, H. Gai, Algorithm Comparison for Real-Time Indoor Environment Digital Twin using BIM, in: 2025: pp. 1137–1141. https://doi.org/10.1109/ISCTIS65944.2025.11065183.

[34] A. Costin, J. Teizer, Utilizing BIM for real-time visualization and indoor localization of resources, in: 2014: pp. 649–656. https://doi.org/10.1061/9780784413616.081.

[35] M. Luo, J. Xie, Y. Yan, Z. Ke, P. Yu, Z. Wang, J. Zhang, Comparing machine learning algorithms in predicting thermal sensation using ASHRAE Comfort Database II, Energ. Buildings 210 (2020), https://doi.org/10.1016/j.enbuild.2020.109776.

[36] K.K. Abbili, Explainable Artificial Intelligence (XAI) and Machine Learning Technique for Prediction of Properties in Additive Manufacturing, J. Adv. Manuf. Syst. 24 (2025) 229–240, https://doi.org/10.1142/S0219686725500118.

[37] S. Lorch, J. Gebele, P. Brune, Towards Trustworthy AI: Evaluating SHAP and LIME for Facial Emotion Recognition, in: 2025: pp. 7534–7543. https://doi.org/10.24251/hicss.2025.900.

[38] Z. Li, Extracting spatial effects from machine learning model using local interpretation method: an example of SHAP and XGBoost, Computers, Env. Urban Sys. 96 (2022), https://doi.org/10.1016/j.compenvurbsys.2022.101845.

[39] M. Shajalal, A. Boden, G. Stevens, Poster: Towards User-centered Explainable Energy Demand Forecasting Systems, in: 2022: pp. 446–447. https://doi.org/10.1145/3538637.3538877.

[40] A.M. Salih, Z. Raisi-Estabragh, I.B. Galazzo, P. Radeva, S.E. Petersen, K. Lekadir, G. Menegaz, A Perspective on Explainable Artificial Intelligence Methods: SHAP and LIME, Adv. Intell. Syst. 7 (2025), https://doi.org/10.1002/aisy.202400304.

[41] H. Lan, H.C. Hou, Z. Gou, A machine learning led investigation to understand individual difference and the human-environment interactive effect on classroom thermal comfort, Build. Environ. 236 (2023), https://doi.org/10.1016/j.buildenv.2023.110259.

[42] Y. Yang, Y. Yuan, Z. Han, G. Liu, Interpretability analysis for thermal sensation machine learning models: an exploration based on the SHAP approach, Indoor Air 32 (2022), https://doi.org/10.1111/ina.12984.

[43] P. Goktas, R. Rakholia, R.S. Carbajo, Answering Key Questions About Air Pollution Dynamics in Ho Chi Minh City: A Spatiotemporal Analysis Using the XAI-SHAP Clustering Approach, in: 2024: pp. 189–203. https://doi.org/10.1007/978-3-031-61069-1_14.

[44] Z. Song, S. Cao, H. Yang, An interpretable framework for modeling global Solar radiation using tree-based ensemble machine learning and Shapley additive explanations methods, Appl. Energy 364 (2024), https://doi.org/10.1016/j.apenergy.2024.123238.

[45] A. Abdellatif, H. Mubarak, H. Ramiah, H. Mokhlis, S. Mekhilef, H.M. Gheni, J. Kanesan, SHapley Additive exPlanations-guided rule-based energy management: bridging machine learning interpretability and adaptive control strategies, Renewable Energy Focus 56 (2026), https://doi.org/10.1016/j.ref.2025.100779.

[46] A. Gani Alam, H. Martin Mathisen, G. Cao, A. Bartonova, B. Ann Kåstad Høiskar, M. F. Fredriksen, Machine Learning Prediction of Student Satisfaction on Indoor Air Quality and Thermal Environment in a Norwegian Secondary School, in: 2025: pp. 596–603. https://doi.org/10.63044/s25pre69.

[47] W. Zhou, M. Yang, X. Yu, Y. Peng, C. Fan, D. Xu, Q. Xiao, Enhancing thermal comfort prediction in high-speed trains through machine learning and physiological signals integration, J. Therm. Biol. 121 (2024), https://doi.org/10.1016/j.jtherbio.2024.103828.

[48] W. Wang, L. Zhu, T. Zhang, X. Zhu, K. Chen, Y. Huo, Integrating local climate considerations into dormitory energy optimization: an explainable machine learning and multi-objective design approach, Urban Clim. 64 (2025), https://doi.org/10.1016/j.uclim.2025.102629.

[49] X. Chen, H. Zhao, B. Wang, B. Xia, Study of Factors Influencing thermal Comfort at Tram Stations in Guangzhou based on Machine Learning, Buildings 15 (2025), https://doi.org/10.3390/buildings15060865.

[50] L. Gugliermetti, F. Cumo, S. Agostinelli, A Future direction of Machine Learning for Building Energy Management: Interpretable Models, Energies 17 (2024), https://doi.org/10.3390/en17030700.

[51] H. Liu, E. Ma, An Explainable Evaluation Model for Building thermal Comfort in China, Buildings 13 (2023) 3107, https://doi.org/10.3390/buildings13123107.

[52] S. Zhang, R. Yao, H. Wei, B. Li, Prediction of occupant thermal state via infrared thermography and explainable AI, Energ. Buildings 312 (2024), https://doi.org/10.1016/j.enbuild.2024.114153.

[53] H. Kim, G. Lee, H. Ahn, B. Choi, Interpretable general thermal comfort model based on physiological data from wearable bio sensors: Light Gradient Boosting Machine (LightGBM) and SHapley Additive exPlanations (SHAP), Build. Environ. 266 (2024), https://doi.org/10.1016/j.buildenv.2024.112127.

[54] X. Li, J. Xu, J. Zhang, T. Tian, R. Xu, Y. Gao, P. Li, X. Zhou, M. Luo, Using SHAP and Machine Learning for Dynamic thermal Comfort Estimation during temperature ramp conditions with infrared camera, Build. Environ. 275 (2025) 112824, https://doi.org/10.1016/j.buildenv.2025.112824.

[55] J. Jiang, Z. Li, K.B. Bedra, C. Long, J. Wu, Q. Zhong, Predicting outdoor thermal comfort in traditional villages: an explainable machine learning framework integrating model optimization, seasonal variability, and tourist-resident insights, Build. Environ. 282 (2025), https://doi.org/10.1016/j.buildenv.2025.113315.

[56] C. Marino, A. Nucara, M. Pietrafesa, Thermal comfort in indoor environment: effect of the solar radiation on the radiant temperature asymmetry, Sol. Energy 144 (2017) 295–309, https://doi.org/10.1016/j.solener.2017.01.014.

[57] Daylight and glazing requirements in new construction, Glass for Europe (2014). https://glassforeurope.com/daylight-and-glazing-requirements-in-new-construction/ (accessed May 26, 2023).

[58] S. Shi, A. Merabtine, R. Bennacer, Radiant vs All-air cooling systems for highly glazed buildings: an experimental study on global and local thermal comfort, Energ. Conver. Manage. 318 (2024) 118900, https://doi.org/10.1016/j.enconman.2024.118900.

[59] S. Shi, A. Merabtine, R. Bennacer, J. Kauffmann, Experimental evaluation of the impact of real sun patch on radiant floor heating in highly glazed spaces, Build. Environ. 244 (2023) 110799, https://doi.org/10.1016/j.buildenv.2023.110799.

[60] A. Psikuta, J. Allegrini, B. Koelblen, A. Bogdan, S. Annaheim, N. Martínez, D. Derome, J. Carmeliet, R.M. Rossi, Thermal manikins controlled by human thermoregulation models for energy efficiency and thermal comfort research – a review, Renew. Sustain. Energy Rev. 78 (2017) 1315–1330, https://doi.org/10.1016/j.rser.2017.04.115.

[61] A. Psikuta, M. Richards, D. Fiala, Single-sector thermophysiological human simulator, Physiol. Meas. 29 (2008) 181, https://doi.org/10.1088/0967-3334/29/2/002.

[62] Z. El akili, Y. Bouzidi, A. Merabtine, G. Polidori, J. Kauffmann, Assessment of thermal comfort of frail people in a sitting posture under non-uniform conditions using a thermal manikin, Build. Environ. 221 (2022), https://doi.org/10.1016/j.buildenv.2022.109334.

[63] Z. El akili, Y. Bouzidi, A. Merabtine, G. Polidori, J. Kauffmann, Thermal comfort of Frail People under dynamic and non-uniform thermal environments using a thermal manikin with thermoregulatory control: an experimental study, Energy and Built Environment 4 (2023) 477–491, https://doi.org/10.1016/j.enbenv.2022.03.005.

[64] Human thermal sensation and comfort in transient and non-uniform thermal environments - ProQuest, (n.d.). https://www.proquest.com/openview/1e8c648fa0725abca2d078fdf0b798d7/1?pq-origsite=gscholar&cbl=18750&diss=y (accessed May 28, 2023).